

# The High-Flux Backscattering Spectrometer at the NIST Center for Neutron Research

A. Meyer<sup>1,2,\*</sup>, R. M. Dimeo<sup>1</sup>, P. M. Gehring<sup>1</sup>, and D. A. Neumann<sup>1†</sup>

<sup>1</sup>*National Institute of Standards and Technology,*

*NIST Center for Neutron Research, Gaithersburg, Maryland 20899-8562*

<sup>2</sup>*University of Maryland, Department for Materials and Nuclear Engineering, College Park, Maryland 20742‡*

(Dated: September 5, 2002 submitted to Review of Scientific Instruments)

We describe the design and current performance of the high-flux backscattering spectrometer located at the NIST Center for Neutron Research. The design incorporates several state-of-the-art neutron optical devices to achieve the highest flux on sample possible while maintaining an energy resolution of less than  $1 \mu\text{eV}$ . Foremost among these is a novel phase-space transformation chopper that significantly reduces the mismatch between the beam divergences of the primary and secondary parts of the instrument. This resolves a long-standing problem of backscattering spectrometers, and produces a relative gain in neutron flux of 4.2. A high-speed Doppler-driven monochromator system has been built that is capable of achieving energy transfers of up to  $\pm 50 \mu\text{eV}$ , thereby extending the dynamic range of this type of spectrometer by more than a factor of two over that of other reactor-based backscattering instruments.

PACS numbers: 61.12.Ex, 61.12.-q

## I. INTRODUCTION

Neutron scattering is an invaluable tool for studies of the structural and dynamical properties of condensed matter. Neutron sources produce neutrons with wavelengths that span the interatomic spacings in solids or the diameter of complex macromolecules, while at the same time having energies that match, respectively, the lattice vibrational frequencies in solids or the slow diffusive motions of atoms. The particular neutron scattering technique known as backscattering [1, 2] is able to resolve energies below  $1 \mu\text{eV}$ , which is well beyond the reach of conventional triple-axis and neutron time-of-flight spectrometers. Thus neutron backscattering spectroscopy is ideally suited to the study of dynamics such as slow motions in complex liquids, jump diffusion, and quantum rotational tunneling.

The principle limitation of backscattering spectrometers has long been the relatively low neutron flux on sample that they produce. This is, of course, a direct consequence of the excellent energy resolution they provide. In this paper we report on the design and performance of the new high-flux backscattering spectrometer (HFBS) located at the NIST Center for Neutron Research that addresses this limitation. Compared to other backscattering spectrometers, the HFBS delivers a higher neutron flux to the sample in large part by the use of a novel device called a phase-space transformation chopper (Sec. III C). In addition, a newly designed Doppler-driven monochromator (Sec. III E), which oper-

ates with a cam machined to produce a triangular velocity profile, extends the dynamic range of the spectrometer by more than a factor of two beyond that of other similar instruments. In a departure from other backscattering spectrometers, the scattering chamber is operated under vacuum instead of in an argon or helium gas environment, which improves the signal-to-background ratio substantially.

## II. BACKSCATTERING

Backscattering spectroscopy exploits the fact that the wavelength spread  $\Delta\lambda$  of a Bragg-diffracted neutron beam decreases as the scattering angle  $2\theta$  approaches  $180^\circ$  (see Fig. 1). This is easily shown [3] by differentiating Bragg's law ( $\lambda = 2d \sin \theta$ ), and then dividing the result by  $\lambda$  to obtain

$$\frac{\Delta\lambda}{\lambda} = \frac{\Delta d}{d} + \frac{\Delta\theta}{\tan \theta}. \quad (1)$$

As  $\theta \rightarrow 90^\circ$  the angular term vanishes. This results in a minimum value of  $\Delta\lambda/\lambda$ , and hence the energy resolution, that depends on the spread  $\Delta d$  and average value  $d$  of the lattice spacing between crystal Bragg planes. In the kinematic limit this minimum is zero. However, dynamical scattering theory shows that the lattice gradient term  $\Delta d/d$  is non-zero, even for perfect single crystals. In this case,  $\Delta d/d$  is given by the Darwin width of the reflection being used to monochromate the neutron beam. [4] This presents a fundamental lower bound for the energy resolution that can be obtained via backscattering, which depends entirely on the structure factor of the reflection being used to monochromate the beam, and the number density of unit cells within the monochromating material. In the backscattering condition the neutron beam is normal to the Bragg planes, corresponding to a Bragg angle

\*Now at Physik Department E13, Technische Universität München, 85747 Garching, Germany

†Corresponding author: dan@nist.gov

‡Always up to date: <http://www.ncnr.nist.gov>

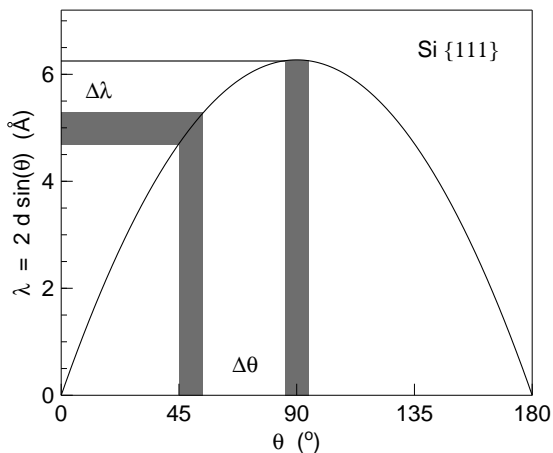


FIG. 1: Illustration of the backscattering principle. Vertical shaded regions correspond to equal angular spreads  $\Delta\theta$ , but vastly different wavelength spreads  $\Delta\lambda$  depending on the Bragg angle  $\theta$ . As  $\theta \rightarrow 90^\circ$ ,  $\Delta\lambda$  (and thus the energy resolution) approaches a minimum.

$\theta = 90^\circ$ . However, the neutron trajectories in a beam are never perfectly parallel. Therefore, some neutrons will strike the crystal Bragg planes at angles slightly less than  $90^\circ$ , thereby satisfying the Bragg condition at different values of  $\lambda$ . Consequently the spread  $\Delta\theta$  in incident angle will also contribute to  $\Delta\lambda$ . [5] Note that  $\Delta\theta$  isn't necessarily (and usually is not) equal to the beam divergence, as it is most often set by the ratio of the source size to the distance between source and Bragg planes. If  $\Delta\theta$  is small, then

$$\frac{\Delta E}{E} = 2 \frac{\Delta\lambda}{\lambda} = 2 \left( \frac{\Delta d}{d} + \frac{1}{8} (\Delta\theta)^2 \right), \quad (2)$$

Most backscattering instruments use the  $\{111\}$  lattice planes of perfect silicon crystals to monochromate the incident beam as well as to analyze the energy of the scattered beam. This is true for the HFBS as well, so for the sake of convenience we define  $\lambda_0 = 2d = 6.2712 \text{ \AA}$ , [6]  $k_0 = 2\pi/\lambda_0 = 1.00 \text{ \AA}^{-1}$ ,  $v_0 = 630.8 \text{ m/s}$ , and  $E_0 = 2.08 \text{ meV}$ . In this case the lattice gradient term  $\Delta d/d = 1.86 \times 10^{-5}$ . As an example of how much the angular spread  $\Delta\theta$  contributes to the energy resolution, one would need a  $\Delta\theta = 0.70^\circ$  to match the lattice gradient contribution to the energy resolution, which is a small angular spread for a neutron beam. Equation (2) would then imply an energy resolution of about  $0.16 \mu\text{eV}$  for the diffracted beam.

The maximum momentum transfer accessible given neutrons of wavelength  $\lambda_0$  is  $Q = 4\pi/\lambda_0 = 2.00 \text{ \AA}^{-1}$ , whereas practical considerations generally limit the minimum useful  $Q$  to  $\sim 0.1 \text{ \AA}^{-1}$  due to the non-zero divergence of the neutron beam incident on the sample. The energy range over which the dynamical properties of a sample can be studied is set by how much the energies of the incident and scattered neutron beams can be shifted relative to each other. This shift cannot be achieved

by varying the Bragg angle of the monochromator, as is often done on a triple-axis spectrometer, because doing so ruins the excellent energy resolution. Instead, energy transfers are obtained using other methods such as varying the temperature of the monochromator with respect to that of the analyzer, resulting in a continuous change in the  $d$ -spacing, [7] or via a Doppler motion of the monochromator crystal, [5] which is the method chosen for the HFBS. Since the analyzer crystals are fixed, a backscattering spectrometer can be compared to a triple-axis instrument operating in a fixed final energy configuration. This is also often referred to as an inverted geometry configuration. Typical backscattering instruments with sub- $\mu\text{eV}$  resolution can reach energy transfers from  $\pm 10$  to  $\pm 15 \mu\text{eV}$  using earlier style Doppler-driven monochromator systems. [8]

### III. GENERAL SPECTROMETER LAYOUT

The design of the HFBS backscattering spectrometer is optimized to provide a large dynamic range and the high-

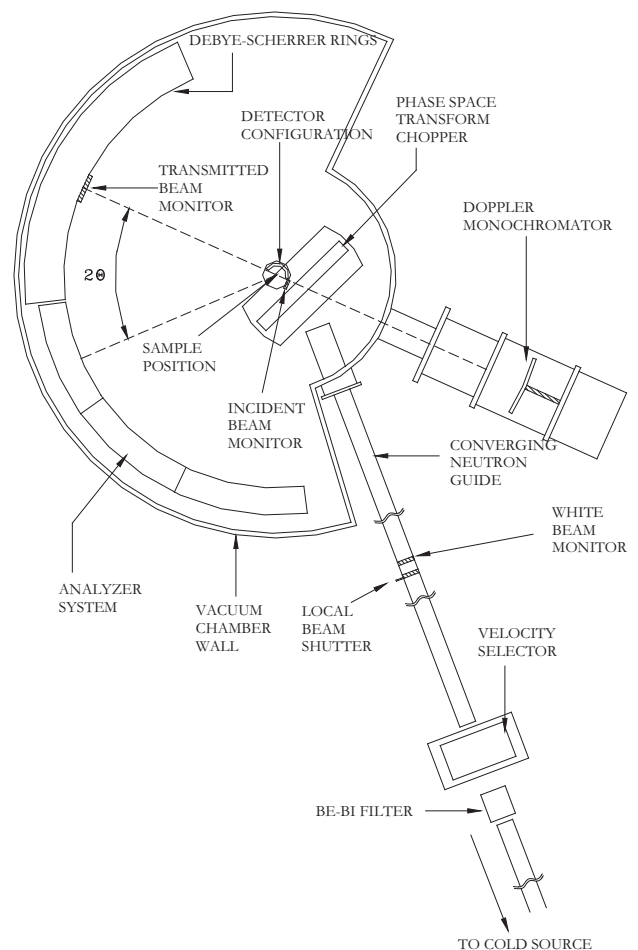


FIG. 2: General layout of the NIST Center for Neutron Research high-flux backscattering spectrometer (HFBS).

est neutron flux on sample possible while maintaining a sub- $\mu\text{eV}$  energy resolution. [9] To achieve these goals the HFBS design incorporates several state-of-the-art neutron optic devices, which are identified in the schematic diagram of the spectrometer shown in Fig. 2. Neutrons from the cold source of the 20 MW NCNR research reactor (Sec. III A) are conducted along a 41.1 m straight neutron guide that is 15 cm high by 6 cm wide, and pass through beryllium and bismuth filters and a velocity selector. A converging guide (Sec. III B), located after the local beam shutter, focuses the neutron beam cross section down to  $2.8\text{ cm} \times 2.8\text{ cm}$ , which enhances the neutron flux by  $\simeq 3.9$ . The neutrons then encounter a phase space transformation (PST) chopper (Sec. III C), a device that Doppler-shifts the incident neutron wavelength distribution towards the desired backscattered wavelength  $\lambda_0$ . The PST chopper provides an additional gain of 4.2 in neutron flux, but at the expense of a sizable increase in divergence. However in doing so the PST chopper alleviates the severe divergence mismatch between the primary and secondary spectrometers, which has been a long-standing problem with backscattering instruments.

Continuing on from the PST chopper, the neutrons are backscattered from a spherically focusing monochromator, strike the sample, and then are backscattered a second time from a spherically focusing analyzer system before they finally reach the detectors. Note that backscattered neutrons must pass through the sample twice. Both the monochromator (Sec. III D) and analyzer (Sec. III F) are composed of large, bent, silicon {111} crystals. These crystals are intentionally bent to increase the lattice gradient term in the energy resolution (see Eq. (2)) in order to obtain a roughly three-fold increase in neutron count rate, while maintaining the sub- $\mu\text{eV}$  energy resolution constraint. Finally, a large energy difference (dynamic range) of up to  $\pm 50\ \mu\text{eV}$  can be established between the monochromated and analyzed beams using a cam-based Doppler drive that produces an oscillatory motion of the monochromator (Sec. III E).

The excellent energy resolution of backscattering instruments comes at the cost of an inherently low neutron flux on the sample. But gains provided by the converging guide, the PST chopper, and the strained silicon monochromator and analyzer crystals help to compensate for this. In addition, the HFBS analyzer stands 2 m tall, spans  $165^\circ$  in  $2\theta$ , and subtends nearly 23% of  $4\pi$  steradians (Sec. III F), making it the largest analyzer of any other backscattering instrument. It is composed of about  $12\text{ m}^2$  of silicon. This large analyzer provides yet another gain over other spectrometers through an increased count rate that is not included by measurements of the neutron flux on the sample. In the following subsections we discuss the various components of the spectrometer in detail starting from the cold source and ending with the detectors. In Sec. IV we report on the performance of the HFBS and present results from several experiments. Recent upgrades and some potential prospects for improvements to the spectrometer are dis-

cussed last in Sec. V.

### A. Neutron Source and Straight Guide

The HFBS is located at the end of a dedicated straight neutron guide, labelled NG-2, that directly views a liquid hydrogen cold source. The cold source exhibits a Maxwellian spectrum with an effective temperature of 37 K for neutrons with wavelengths  $4\ \text{\AA} \leq \lambda \leq 15\ \text{\AA}$ . [10] The flux at the backscattered wavelength  $\lambda_0$  is estimated to be  $\sim 1.2 \times 10^{11}\text{ n}(\text{cm}^2\text{ s Sr \AA})^{-1}$ . Neutrons from the cold source reach the HFBS by traveling along an evacuated glass guide 41.1 m in length with a constant 15 cm high by 6 cm wide cross section. The interior top and bottom surfaces of the guide are coated with NiCTi supermirrors, which have a critical angle for reflection given by  $\theta_c = Q_c\lambda = 0.044\lambda\ \text{\AA}^{-1}$ . The interior side surfaces of the guide are coated with  $^{58}\text{Ni}$ -equivalent supermirrors for which  $\theta_c = 0.026\lambda\ \text{\AA}^{-1}$ . [11]

An 87 cm long gap interrupts the straight guide 26.3 m downstream from the cold source to provide space for filter material and a velocity selector. These elements are necessary because the HFBS design places the sample position and detectors in close proximity to a direct line of sight with the reactor core. The estimated loss of  $\lambda_0$  neutrons from this gap is  $\approx 15\%$ . Three blocks of vacuum-cast polycrystalline beryllium and one block of “pseudo” single-crystal bismuth, each 10 cm in length and  $16.5\text{ cm} \times 6.4\text{ cm}$  in cross section, are used to remove fast neutrons and suppress core gamma-ray ( $\gamma$ -ray) radiation. [12] Vacuum-cast beryllium is known to produce half the beam broadening for a given length of filter at a given wavelength than does the hot-pressed grade of beryllium. [13] This implies fewer neutrons will be lost through the guide walls downstream after they have passed through the filter. The filters are also cooled within a liquid nitrogen dewar to minimize the effects of thermal diffuse scattering and maximize the transmission of cold neutrons. Using this 40 cm combination of beryllium and bismuth filter material, the respective transmission of core  $\gamma$ -rays ( $E \geq 2\text{ MeV}$ ), and fast ( $E \geq 2\text{ MeV}$ ), epithermal ( $E \sim 1\text{ eV}$ ), and cold neutrons are estimated to be 0.20%, 0.06%,  $2 \times 10^{-9}\%$ , and 53%. (The estimate for the cold neutron transmission includes the gap loss of 15%.)

The neutron velocity selector, placed just after the two filters, is used to limit  $\Delta\lambda/\lambda$  to 18%. This minimizes the background produced by neutrons having wavelengths that lie outside the bandwidth accepted by the PST chopper. The blades of the velocity selector have an axial length of 30 cm, and are composed of 0.4 mm thick carbon-fiber in epoxy loaded with  $^{10}\text{B}$  as absorber material. This gives a relative suppression of unwanted neutrons of  $2 \times 10^{-4}$ . The velocity selector was designed to accept the entire  $15\text{ cm} \times 6\text{ cm}$  neutron guide cross-section. This posed a technical challenge because the blades had to have a large enough diameter to accom-

modate the 15 cm vertical dimension of the guide, yet be able to move at high speeds. To achieve a peak neutron transmission centered at  $\lambda_0$ , the velocity selector must rotate at 16200rpm, which corresponds to a tangential speed of 410m/s at the edge of the blades. The peak transmission of the selector at this wavelength is 83%.

A standard gold foil activation analysis was performed along the key points of the guide with the NIST reactor operating at full power (20 MW). This analysis assumes a cross section of 98.65 barns for thermal neutrons with wavelength  $\lambda = 1.8 \text{ \AA}$ . Just upstream of the filters, the thermal capture flux equivalent was measured to be  $3.37 \times 10^9 \text{ cm}^2/\text{sec}$ . [14] After the filters and the velocity selector, the thermal capture flux is  $1.57 \times 10^9 \text{ cm}^2/\text{sec}$ , [14] which corresponds to a net transmission of about 44%. This value is consistent with the losses estimated for the guide cut and the filter and velocity selector transmissions.

### B. Converging Guide

A converging guide is used to focus the large guide beam cross section down to a size that is commensurate with typical sample dimensions. The guide entrance is located 41.3 m downstream from the cold source, just after the local beam shutter, and before the PST chopper. All four of its interior surfaces are coated with  $2\theta_c^{\text{Ni}}$ -equivalent ( $Q_c = 0.044 \text{ \AA}^{-1}$ ) supermirrors, which compress the beam cross section from  $15 \text{ cm} \times 6 \text{ cm}$  down to  $2.8 \text{ cm} \times 2.8 \text{ cm}$ . Acceptance diagrams [15, 16] were used to determine the optimal guide length and distances over which the vertical and horizontal focusing should occur. In this context “optimal” does not necessarily imply the largest gain factor (although the resulting gain is still quite good). Instead, our design goal was to maximize the gain subject to the constraint that the resulting phase space elements corresponding to different reflections remain “compact,” or bunched tightly together. In so doing one avoids the presence of gaps in the divergence of the subsequent neutron beam seen by the PST chopper.

Based on these considerations, the vertical focusing was designed to take place over a 4 m guide length, while the focusing in the horizontal direction occurs over only the last 3 m. The resulting acceptance diagrams are shown in Fig. 3 for  $\lambda = \lambda_0$  assuming a uniform illumination of the guide entrance, and a perfect reflectivity for the supermirror coatings for  $0 \leq Q \leq Q_c$ . Elements that correspond to zero and one reflection from the converging guide walls are represented by the solid and hatched regions, respectively. The tiny, isolated wedge-shaped elements that appear in the horizontal case arise from neutrons that undergo two reflections. These acceptance diagrams were calculated analytically. As a cross check, Monte Carlo simulations of the straight guide + converging guide system were performed, and these yielded acceptance diagrams that agreed extremely well with those shown in Fig. 3.

The performance of the converging guide is characterized by the uniformity of the beam profile exiting the guide, and by the flux gain. To quantify these two parameters, autoradiograph images of the beam before and after guide were obtained by irradiating (independently) two separate  $\sim 125 \mu\text{m}$  thick Dy foils ( $1 \mu\text{m} = 10^{-6} \text{ m}$ ). The beam intensity was then integrated over 9 (5) different circular regions on the autoradiograph taken before (after) the guide, with the regions in each case representing slightly less than 2% of the total beam cross sectional area. These intensities vary by 7% or less, indicating a highly uniform beam profile at both guide positions. [9] The measurements also indicate a flux gain of 3.43, somewhat higher than the value of 3.1 predicted by the acceptance diagram calculations. By contrast, a larger flux gain of 3.33 is predicted by the Monte Carlo simulations which take into account neutrons lost in the 87 cm guide

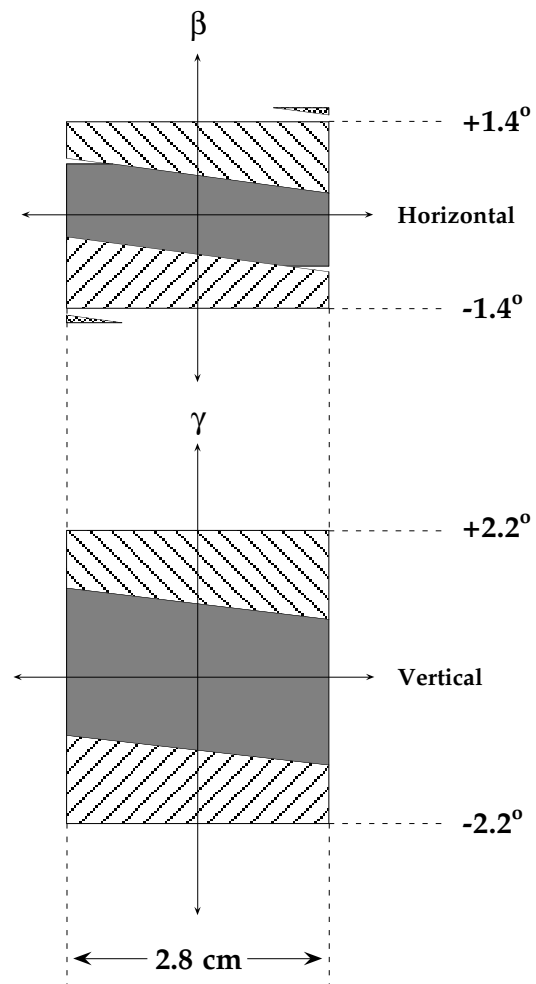


FIG. 3: Acceptance diagrams for  $\lambda_0$  neutrons exiting the converging guide. Top panel: horizontal divergence  $\beta$  versus lateral guide dimension. Bottom panel: vertical divergence  $\gamma$  versus vertical guide dimension.

cut which otherwise would have entered the converging guide, but would have been lost in the walls.

Gold foil activation measurements were made at the entrance and exit of the guide to obtain a more accurate value of the flux gain, and the corresponding thermal neutron capture fluxes were  $2.13 \times 10^8 \text{ n (cm}^2 \text{ sec)}^{-1}$  and  $8.29 \times 10^8 \text{ n (cm}^2 \text{ sec)}^{-1}$ , respectively. [9, 14] Both values are accurate to within 1% assuming an uncertainty of one standard deviation based on counting statistics. The resulting flux gain is then 3.89, higher than both the calculated value and that obtained from the autoradiograph images. This discrepancy motivated, in part, a subsequent check of the reflectivity of the straight guide coatings, where additional superstructure in the reflectivity of the  $^{58}\text{Ni}$ -equivalent supermirror coatings was found beyond the presumed critical wave vector of  $Q_c = 0.026 \text{ \AA}^{-1}$ . Incorporating the results of the reflectivity studies on the guide supermirror coatings into the simulations was then sufficient to reconcile the discrepancy between the experimental and calculated gains entirely. [17]

The divergence of the neutron beam exiting the converging guide has not been measured experimentally. However, Monte Carlo simulations of the angular distributions of neutrons exiting the converging guide were done that took into account the non-zero bandwidth transmitted by the velocity selector. Figure 4 shows the results of these simulations, where  $N(\theta)$  is the total number of neutrons exiting the guide with a horizontal (vertical) divergence  $\theta$  with respect to the beam axis. The vertical axes have been scaled such that the two integrated

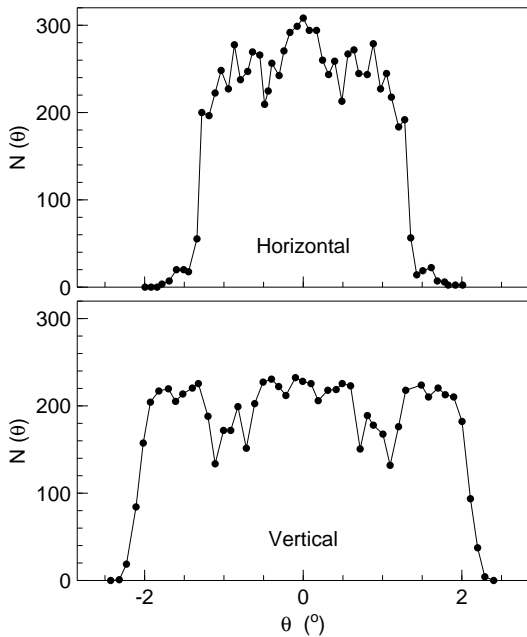


FIG. 4: Monte Carlo simulations of the angular distributions of neutrons exiting the converging guide in the horizontal and vertical directions. (Simulations are courtesy of J. C. Cook.)

distributions are equal (i. e. contain the same number of neutrons), but otherwise the units are arbitrary. The distributions at the exit of the guide are found to be reasonably uniform in both the horizontal and vertical directions.

### C. Phase Space Transformation Chopper

Backscattering spectroscopy is inherently a flux-limited technique because of the narrow energy resolution it provides. To help boost the low count rates, most spectrometers employ a rather poor  $Q$ -resolution that is introduced by the focusing analyzer system, which compresses large regions of solid angle into few detectors. However, all cold neutron backscattering instruments at steady state sources are located on neutron guides, the coatings of which limit the divergence of the beam fed to the monochromator system. This then creates a situation that effectively defeats the purpose of the focusing analyzer in that the monochromator system cannot supply a beam with sufficient divergence to take full advantage of the large angular acceptance of the analyzer system. Thus the opportunity exists to increase backscattering count rates, without adversely affecting the performance of the instrument, if one can design a primary spectrometer capable of generating a highly divergent beam from that supplied by the guide. To accomplish this, Schelten and Alefeld proposed the idea of neutron phase space transformation (PST) using moving mosaic crystals. [18]

The phase space transformation process is outlined schematically in Fig. 5. Panel (a) depicts an incoming, well-collimated “white” beam, similar to that which exits a neutron guide, as an element in phase space. Each point in this element corresponds to a neutron with an incident wave vector  $k_i$  measured relative to the origin. After diffracting from a stationary mosaic crystal, the phase space element is transformed into the concave-shaped element shown on the right. No neutron energies are changed in this process, so there is no change in the number of neutrons in a given wavelength band. The situation changes, however, if the crystal is set in motion along a direction perpendicular to the average scattering vector, and antiparallel to the projection of  $k_i$  onto the crystal Bragg planes as shown in panel (b). In this case the concave element rotates in phase space, and this *does* change the neutron energy distribution. More importantly, the rotation is such that shorter wave vectors become elongated while longer wave vectors are shortened, thereby “bunching” up the wave vectors of the diffracted neutrons about the desired backscattered value  $k_0 = 1.00 \text{ \AA}^{-1}$ . Thus the number of neutrons in a given wavelength band can be increased via phase space transformation. It is possible to carry this process too far by moving the mosaic crystals too quickly. In this case the outgoing phase space element rotates too much, and the desired “bunching” effect reverses (Fig. 5(c)).

It can be difficult to understand how the phase space

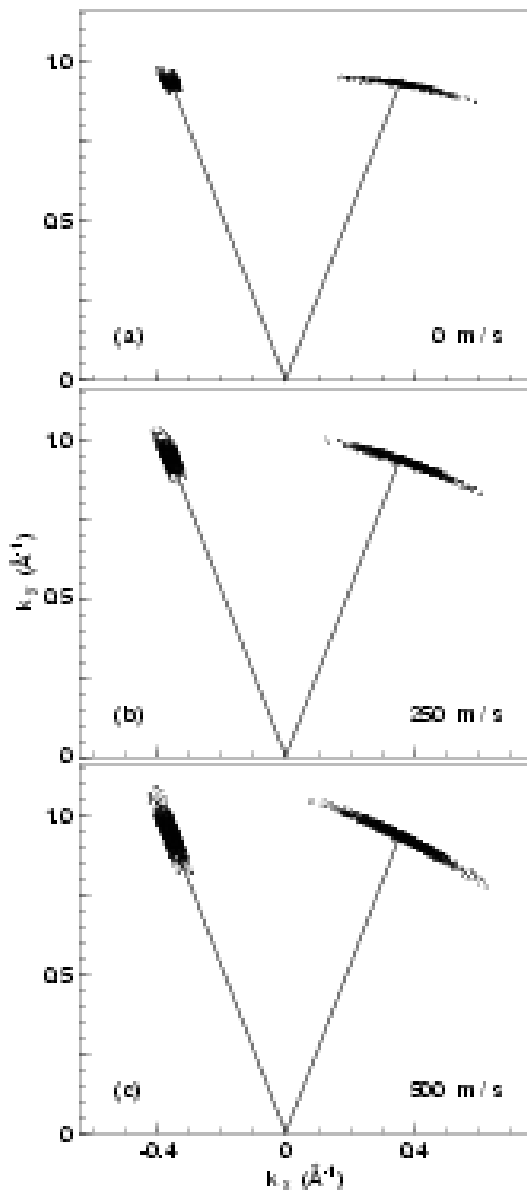


FIG. 5: Simulations of the phase space transformation process using 0.5 cm thick HOPG crystals with an intrinsic mosaic spread of  $5^\circ$  FWHM. The different panels correspond to tangential crystal speeds of (a) 0 m/s, (b) 250 m/s, and (c) 500 m/s. The simulations are three-dimensional projections onto the  $(k_x, k_y)$  plane.

transformation process works. An intuitive explanation can be given in real space keeping in mind the mosaic nature of the crystalline Bragg planes, as well as the tight divergence of the incident beam. The slower moving neutrons incident on the PST chopper HOPG crystals must find mosaic blocks oriented at higher angles in order to satisfy the Bragg condition. Therefore they get a “push” from the moving crystal. By contrast, the faster neutrons satisfy the Bragg condition at smaller angles, so diffraction occurs from crystallites oriented in the opposite sense, thereby reducing their speed. The net effect of

this process is the remarkable conversion of the incoming spread in neutron wave vector (i. e. energy) into a corresponding outgoing angular spread, precisely the requirement for increasing the count rate of a backscattering spectrometer. This transformation process is necessarily consistent with Liouville’s theorem which requires that the volumes of the incoming and outgoing phase space elements be identical.

Because the HFBS monochromates and energy-analyzes neutrons using the (111) reflection of Si, the PST chopper has been designed to enhance the neutron flux at the corresponding backscattered energy  $E_0$ . As implemented on the HFBS, the device consists of a 1 m diameter disk whose periphery is divided into six sectors. Alternate sectors are covered with crystals of highly-oriented pyrolytic graphite (HOPG) that are 34.5 mm tall, 1.5 mm thick, and mounted inside protective cassettes. These cassettes clamp the crystals firmly in place to prevent any movement which would certainly damage the crystals given the high speeds they experience. Finally, the chopper disk is mounted such that the axis of rotation is parallel to the average graphite scattering vector. Figure 6 is a photograph of the PST chopper inside its casing that shows the three cassettes which contain and protect the 180 HOPG crystals. The design of the PST chopper obviously introduces a pulsed-structure to the diffracted neutron beam, a fact that is exploited to good advantage by the data acquisition system described in Sec. III.

Graphite is an ideal choice of crystal for the PST chopper because the  $d$ -spacing of the (002) planes is 3.355 Å, which is slightly larger than the 3.135 Å  $d$ -spacing of the Si (111) reflection used to monochromate the neutrons. This means that neutrons that satisfy the backscattering condition will be diffracted from the PST chopper at a Bragg angle of  $69.2^\circ$ , which allows for the convenient placement of the monochromator relative to the converging guide (see Fig. 2). Moreover high-quality HOPG crystals having the requisite mosaic are readily available, and



FIG. 6: Photograph of the PST chopper with the front casing removed. The chopper disk and the three cassettes which contain the HOPG crystals are exposed. The distance between the axis of rotation and the center of the crystals is 505 mm.

the HOPG neutron reflectivity is quite good. [19] Based on results from the analytical calculations and Monte Carlo simulations reported in Appendix A, the effective FWHM mosaic of the graphite was chosen to be  $7.5^\circ$ . This mosaic was obtained by sandwiching three crystals, each having a mosaic between  $2.25^\circ$  and  $3.00^\circ$ , between wedge-shaped spacers. This approach has the advantage of limiting the vertical mosaic to that of an individual crystal, or about  $2.5^\circ$ , and hence the vertical divergence. This is an important consideration from a design standpoint for two reasons. First, the vertical divergence determines the height of the monochromator. Second, given the high accelerations reached by the Doppler drive (see Sec. III E), the mass of the monochromator must be kept as low as possible, and a larger height will imply a larger mass.

A linear crystal speed of 250 m/s was chosen, again based on the calculations described in Appendix A. At this speed the analytical and Monte Carlo results predict gains of 6.7 and 5.0, respectively, given the incident neutron distributions produced by the guide system described earlier. To achieve a speed of 250 m/s, the PST chopper must rotate at 4,730 rpm. Note that the choice of chopper radius (0.505 m), rotational frequency (79 Hz), and number of cassettes all depend on the speed of  $\lambda_0$  neutrons (630.8 m/s) and the nominal distance between the monochromator and the PST chopper (2 m). This is because of the critical timing issue whereby the HOPG crystals must rotate fully out of the monochromated beam path by the time the neutron pulse diffracted from the PST chopper and then backscattered from the monochromator returns to the PST. With the aforementioned parameters, the PST chopper rotates by approximately  $180^\circ$  in this time, thereby allowing the now monochromatic neutron beam to pass through an open segment in the chopper on its way to the sample.

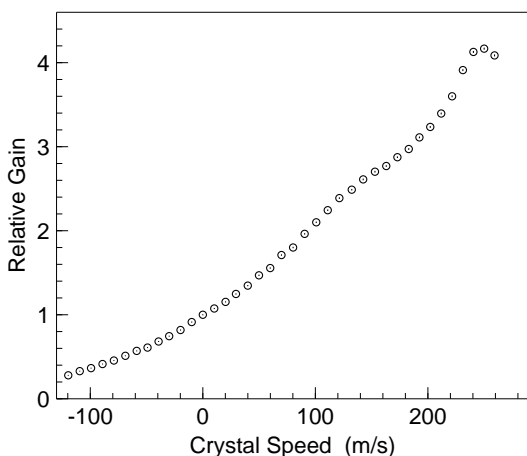


FIG. 7: Relative flux gain as a function of the tangential speed of the HOPG crystals in the PST. At the operating speed of 250 m/s (4730 rpm), the PST chopper gives a maximal increase in neutron flux of 4.2 compared to the chopper at rest.

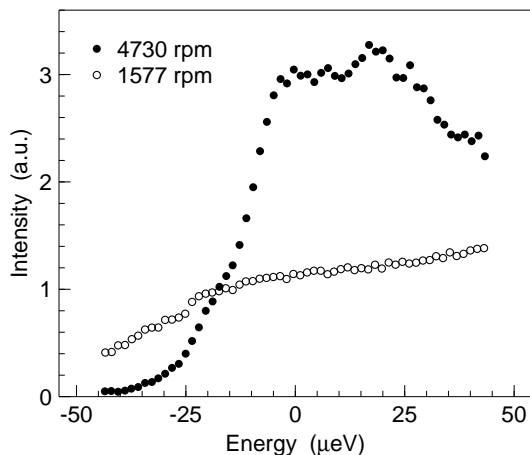


FIG. 8: Neutron beam intensity as a function of energy transfer, measured with the incident beam monitor for two different operating speeds of the PST.

Because of this timing constraint, the PST chopper fully transmits the monochromated neutron pulses at several discrete frequencies only. In addition to 4,730 rpm, the HFBS can function with the PST chopper rotating at 1/3rd speed, or 1,577 rpm. To avoid these timing issues during the initial performance tests of the PST chopper, measurements of the relative neutron flux as a function of crystal speed were made by placing a detector directly on top of the PST chopper casing, i. e. slightly out of the backscattering condition. These measurements were performed in the fall of 1997, and are shown in Fig. 7. The measured gain at the operating velocity of 250 m/s is 4.2, somewhat reduced from the calculations, but still quite substantial. The HFBS is the first neutron spectrometer to incorporate a PST chopper.

A very important finding of the PST chopper simulations is that the diffracted energy bandwidth has a FWHM of roughly  $80 \mu\text{eV}$ . Thus large energy transfers  $\Delta E$  will come at the price of a reduced flux on the sample, particularly at the extremes of the dynamic range. Because the simulations show that the distribution of energies reflected from the PST chopper is somewhat skewed to energies greater than  $E_0 = 2.08 \text{ meV}$ , this reduction should be more pronounced for incident energies less than  $E_0$ . Fig. 8 displays the flux as a function of energy transfer  $\Delta E = E_i - E_f$  as recorded by the incident beam monitor which is mounted between the PST chopper and the sample. A similar spectrum is collected for every data file and is used to normalize the scattered intensity to the incident flux. As expected from the simulations, one sees that the number of neutrons incident on the sample decreases as the incident energy deviates from 2.08 meV. Moreover, in qualitative agreement with the simulation, this reduction is substantially more severe for incident energies less than  $E_0$  compared to those greater than 2.08 meV. Further details of the phase space transformation process are provided in Appendix A.

#### D. Monochromator

Figure 9 shows a photograph of the HFBS monochromator which is 52 cm wide by 28 cm tall, and spherically curved to a radius of 2.12 m. This radius of curvature is required to focus the neutrons diffracted by the PST chopper (2 m away) onto the sample which sits 2.25 m from the monochromator. The monochromator is composed of  $\sim 15$  hexagonal Si {111} wafers, each  $750 \mu\text{m}$  thick, glued onto the concave surface of a support structure. Details regarding the choice of crystal thickness are given in Sec. III F which discusses the design of the analyzer. The support structure is made of a graphite composite with a foam core to minimize the total mass (0.74 kg without crystals, 0.95 kg with crystals and support shaft). It is designed to deflect no more than 0.25 mm at the highest Doppler drive speed because large deflections would broaden the energy resolution. The two-component epoxy used to attach the silicon wafers to the support was selected for its durability under dynamic loading conditions. The wafers were originally glued onto the monochromator support using a single-component anaerobic retaining adhesive widely used in the automotive industry. However, during the initial commissioning phase of the spectrometer there were numerous adhesive failures, particularly at high monochromator speeds. These resulted in the catastrophic loss of many wafers and prompted the search for an alternative. The two-component epoxy has proven to be very reliable, and there have been no failures since its first use.

A large monochromator width is needed to span most of the neutron beam diffracted from the PST chopper which, as a consequence of the phase space transformation process, has a much larger horizontal divergence ( $\sim 15^\circ$ ) compared to that of the beam exiting the converging guide ( $\sim 2.8^\circ$ ). The width of the monochromator was specifically chosen so that it would capture the FWHM of the neutron beam diffracted from the PST chopper. Assuming a Gaussian angular distribution for the diffracted beam, this width is sufficient to intercept nearly 80% of the neutrons arriving at the monochromator position. By comparison, to intercept 95% of the beam would require a monochromator width of more than 85 cm, which is impractical due to the mass limitations imposed by the Doppler drive.

Measurements were performed to verify that most of the neutrons arriving from the PST chopper do indeed strike the monochromator. These were done by sequentially masking all but the left, middle, and right thirds of the monochromator surface with a neutron absorbing material, and then measuring the neutron intensity scattered by a standard vanadium sample with the Doppler drive operating at low speed. These measurements indicate that more than 40% of the monochromatic neutrons that scatter from the sample come from center third of the monochromator. This is consistent with the value of 40% expected for a Gaussian distribution truncated at half-maximum. Measurements of the neutron intensity



FIG. 9: Photograph of the HFBS monochromator, which is composed of Si {111} wafers glued to a light-weight, but rigid, graphite composite structure with a foam core.

produced by the left and right thirds of the monochromator are symmetric, and also consistent with what is expected for a Gaussian distribution ( $\sim 30\%$  on either side).

Additional measurements were made with the monochromator divided vertically into thirds. These results indicate that roughly 50% of the neutrons that strike the sample come from the center third of the monochromator, while approximately 25% come from each of the thirds above and below the center. If one assumes a vertical Gaussian distribution (which is consistent with these results), then these measurements suggest that the monochromator is tall enough to accept more than 95% of the neutrons leaving the PST chopper. When taken together, the vertical and horizontal measurements indicate that the monochromator is large enough to accept  $\sim 75\%$  of the neutrons that leave the PST chopper. In fact, since the simulations described in Appendix A indicate that the angular distribution of neutrons is truncated, we believe that the fraction of neutrons that impinge on the monochromator is actually somewhat greater than 75%.

#### E. Doppler Drive

The HFBS employs a mechanical Doppler drive to produce an oscillatory motion of the monochromator that is used to doppler shift the neutron energies incident on the sample about the average value  $E_0$ . The motion of the monochromator is oriented along the average silicon wafer [111] direction. In this manner the backscattering condition is always maintained, thereby preserving the desired sub- $\mu\text{eV}$  energy resolution. Many authors have discussed Bragg diffraction from moving lattices in detail. [20, 21] Backscattering from a moving monochromator is a special case of this for which the neutron velocity is parallel to the motion of the crystal Bragg planes. In this case, the energy shift of backscattered neutrons rel-



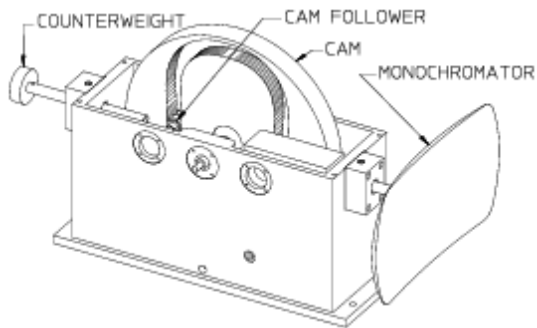


FIG. 10: Internal schematic view of monochromator doppler drive and cam system. From Gehring and Neumann. [9]

ative to  $E_0$  is given by

$$\Delta E = E_m - E_0 = 2E_0 \left( \frac{v_m}{v_0} \right) + E_0 \left( \frac{v_m}{v_0} \right)^2, \quad (3)$$

where  $v_m$  is the velocity of the monochromator.

In contrast to other backscattering spectrometers, the HFBS employs a cam-based Doppler drive system to vary the incident energy  $E_i$  (see Fig. 10). The velocity profile is determined uniquely by the shape of the cam, which is machined from tool steel and then heat treated. The monochromator is connected through a shaft to bearings that follow the contours of the cam, thereby converting the rotational motion of the cam into an oscillatory linear motion. A counterweight of equal mass is driven in opposition by the same method to maintain the dynamical balance of the Doppler drive system. The dynamic range of the spectrometer is set by the frequency of the Doppler drive for a given cam. Cams with triangular and sinusoidal velocity profiles have been tested on the HFBS. Both have certain advantages over the other. A triangular velocity profile is desirable because the linear portions weight all energy transfers equally in time. A sinusoidal waveform, on the other hand, spends more time at the maximum speeds, thereby weighting higher energy transfers more heavily. This can be useful when the signal is weaker at large energies. The more commonly used crank-shaft driven Doppler systems produce a close approximation to a sinusoidal velocity profile. [8].

Figure 11 shows the triangular and sinusoidal velocity profiles for each cam as measured using a laser vibrometer. A small polished area in the center crystal of the monochromator reflects the light from the laser vibrometer. The doppler-shifted light is compared to an internal reference signal by the vibrometer which uses the difference to generate an extremely accurate analog output that is directly proportional to the instantaneous velocity of the monochromator. The profiles in Fig. 11 correspond to a frequency of 4.94 Hz, or roughly a range of  $\pm 10 \mu\text{eV}$  in energy transfer. The velocity dependence of the triangular cam is linear in time over almost the entire cycle. In addition, the triangular cam gives a 19% larger dynamic range at the same frequency than does the sinusoidal cam. Interestingly, some “ripples” are clearly

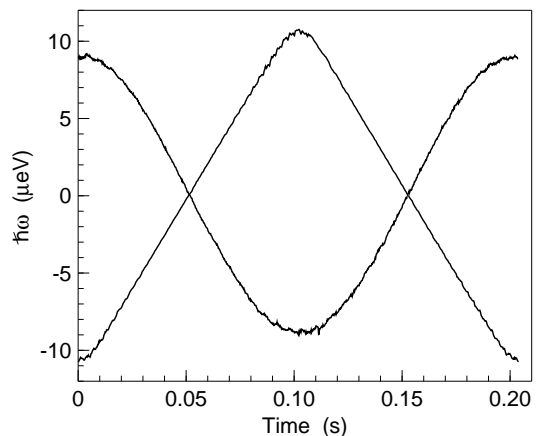


FIG. 11: Velocity profiles of the monochromator during one cycle of the Doppler drive running at 4.94 Hz. The two profiles, one using the triangular cam, and one using the sinusoidal cam, were measured with a laser vibrometer. The sinusoidal profile has been multiplied by -1 for ease of comparison. Compared to the sinusoidal cam the triangular cam provides large regions of linear velocity dependence, and a larger dynamic range at a given frequency.

evident at higher energy transfers in both velocity profiles. The ripples are real, and are attributed to the motion of the bearings in the cam that result from the non-zero machining tolerances. These ripples are an intrinsic feature of any cam-based Doppler drive and can not be suppressed completely. However the vibrometer signal is highly localized, only reflecting the motion of the center of the monochromator. In fact the neutrons sample the entire  $1500 \text{ cm}^2$  surface area. Since the monochromator support is not perfectly stiff, the ripples are not coherent over the surface area. Thus the effects of the ripples are smeared out in the reflected neutrons. As will be seen in Sec. IV, they produce no detectable effects on the energy spectra.

The Doppler drive is designed to achieve a top frequency of 25 Hz corresponding to monochromator accelerations in excess of  $100 g$ . This not only poses the problem of keeping the crystals attached to the monochromator support, but it also implies significant vibrations of the Doppler drive at high frequencies. Measurements made with an accelerometer indicate a number of pronounced resonant frequencies at which the Doppler drive should not be operated. The vibrations in the Doppler

Monochromator Frequency	Dynamic Range	Energy Resolution
4.9 Hz	$\pm 11 \mu\text{eV}$	$0.80 \mu\text{eV}$
9.0 Hz	$\pm 20 \mu\text{eV}$	$0.87 \mu\text{eV}$
16.2 Hz	$\pm 36 \mu\text{eV}$	$1.01 \mu\text{eV}$

TABLE I: Instrumental elastic energy resolution as a function of dynamic range.

drive create a distribution of velocities of the monochromator around  $E_0$ , and therefore lead to a broadening of the instrumental energy resolution. For example, a measurement at 21 Hz ( $\Delta E = \pm 46.7 \mu\text{eV}$ ) gives an asymmetric instrumental energy resolution function with a width of about  $4 \mu\text{eV}$  (FWHM). There are several operating frequencies at which this broadening is minimized as shown in Table I.

### F. Analyzer

Figure 12 shows a photograph of the HFBS analyzer. The analyzer consists of 8 spherical “orange peel”-shaped sections that stand 201 cm tall by 36.4 cm wide (at the center). Together these sections give an approximately continuous coverage over scattering angles  $2\theta$  ranging from  $39.3^\circ$  to  $124.3^\circ$ . For lower angles, four Debye-Scherrer rings cover  $7.8^\circ \leq |2\theta| \leq 39^\circ$ . At a coverage of nearly 23% of  $4\pi$  steradians, the HFBS analyzer is the larger than that of any other backscattering instrument. The analyzer radius of curvature is 2.05 m, instead of 2 m, so that backscattered neutrons are focused onto the detectors rather than onto the sample. This allows for a smaller entrance window into the detector assembly, and thus a reduced background, but at a cost of a small increase in energy resolution and a slightly asymmetric shape to the instrumental energy resolution function.

An important gain in intensity is obtained by gluing large diameter ( $\sim 120$  mm) Si {111} wafers onto both the monochromator and the analyzer support structures because bending increases the intrinsic lattice gradient of silicon beyond its Darwin limit. This results in more flux at the expense of an increased instrumental energy resolution. The amount by which  $\Delta d/d$  changes with bending depends on both the radius of curvature  $R_c$  and the crystal wafer thickness  $t$  according to the expression

$$\frac{\Delta d}{d} = \left(\frac{\Delta d}{d}\right)_{\text{Darwin}} + P_{\text{eff}} \left(\frac{t}{R_c}\right), \quad (4)$$

where  $P_{\text{eff}}$  is an effective Poisson’s ratio which, for spher-



FIG. 12: Photograph of the HFBS analyzer with technician S. Slifer kneeling to inspect the alignment.

ically bent Si {111}, is about 0.44. [21]

The preceding equation predicts that a thickness of only  $150 \mu\text{m}$  is sufficient to obtain an energy resolution of  $0.75 \mu\text{eV}$  FWHM, which satisfies the HFBS sub- $\mu\text{eV}$  constraint. However, the effect of a significant bending strain on the reflectivity of perfect silicon crystals was not known. Therefore two sets of extensive tests were carried out at the Institut Laue Langevin on the backscattering spectrometer IN16 using small analyzer prototypes composed of wafers with thicknesses from 250 to  $950 \mu\text{m}$  to determine the optimal wafer thickness experimentally. The results of these measurements indicated a much weaker dependence of the energy resolution on the wafer thickness  $t$ . Moreover, as shown in Fig. 13, it was observed that silicon thicknesses less than  $700 \mu\text{m}$  did not fully saturate the reflectivity. Based on these results a value of  $750 \mu\text{m}$  was chosen for the thickness of the silicon wafers covering both the monochromator and analyzer. In addition, it was found that chemically etching the wafers gave a highly Gaussian shape to the resolution function, whereas unetched wafers resulted in an additional strong Lorentzian component. Hence all wafers used to make the HFBS analyzer and monochromator were chemically etched after cutting (but not polished). [22]

That such thick wafers are needed to saturate the neutron reflectivity is surprising. The primary extinction length [23] for the (111) reflection of silicon is only  $34.2 \mu\text{m}$ . Popovici later pointed out that for small deflections, a wafer simply bends and the strain remains zero in the middle (neutral) layer. [24] The reflectivity will then saturate as long as this neutral layer is thicker than the primary extinction length. But when the deflection exceeds roughly half the wafer thickness, which happens very soon with thin wafers, this neutral layer becomes strained. The wafer stretches non-uniformly on bending and the lattice gradient changes drastically, thereby

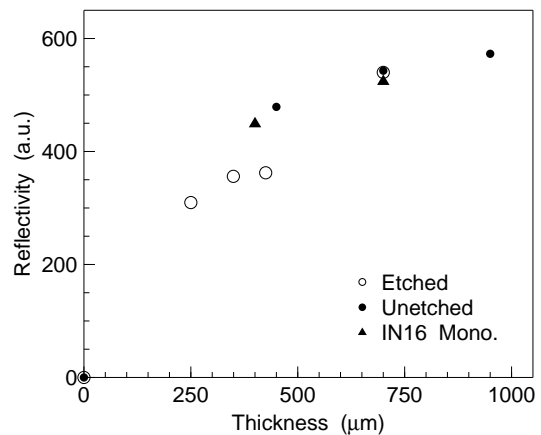


FIG. 13: Plot of neutron reflectivity versus Si {111} wafer thickness. Open circles represent etched wafers, while solid circles represent unetched wafers. The solid triangles refer to the two IN16 monochromators.

altering the primary extinction length.

The stretching should result not just in a spread of  $d$ -spacings, but also in a non-uniform change in the nominal  $d$ -spacing, which in backscattering will matter. One then has to increase the thickness in order to return to an unstrained middle surface, and thus to a good reflectivity. Given  $R_c = 2.05$  m, and an effective wafer “diameter” of order 102 mm (the wafers are hexagonal), the resulting deflection is about 0.63 mm. Based on this argument, the wafer thickness should exceed 1.2 mm in order to be larger than twice the deflection. Our experimental tests show that such thick wafers are not necessary to saturate the reflectivity. However they do convincingly demonstrate the validity of the premise that the neutral layers in a thin crystal wafer are drastically affected by bending.

### G. Detector Assembly

Neutrons backscattered from the analyzer must pass through the sample a second time in order to reach the detectors, which are located on a 10 cm radius centered on the sample position (see Fig. 2). A radial collimator, composed of 3 cm long cadmium fins sandwiched between each detector, sits between the sample and detectors to reduce the background and suppress spurious scattering from the sample environment. The HFBS detector assembly consists of 12 12.27 mm diameter pencil-style detectors, each with a  $^3\text{He}$  fill pressure of 6 bars. The detectors are located at positions corresponding to scattering angles of  $32.3^\circ \leq 2\theta \leq 121.25^\circ$ , or momentum transfers of  $0.56 \leq Q \leq 1.75 \text{ \AA}^{-1}$  respectively. Each detector has an angular acceptance of  $7.75^\circ$ , which is about half the horizontal divergence of the neutron beam. The PST chopper housing partially shadows the analyzer at large scattering angles resulting in a reduced count rate in the detectors at  $Q = 1.68 \text{ \AA}^{-1}$  and  $Q = 1.75 \text{ \AA}^{-1}$ .

A picture of the sample area taken from within the HFBS vacuum chamber is shown in Fig. 14. The detector assembly appears on the left-side of the cylindrical sample insert, and is shielded by a cadmium and boronated-aluminum frame. The assembly and frame are electrically isolated, and mounted onto a metal plate attached to a stand-alone post that can be rotated away from the sample insert to facilitate testing and repairs. The large circular outline of the PST chopper is visible behind the sample insert, and the chopper window through which the main guide and monochromated beams pass is outlined in black. The shiny square-shaped metal piece to the left of the detector assembly is the end of the beam stop for the main guide. At right one can see a few of the hexagonal silicon crystals comprising the high-angle portion of the analyzer. The shadowing of this portion of the analyzer by the PST chopper is evident.

Three additional rectangular-shaped detectors with  $^3\text{He}$  fill pressures of 2.5 bar and a  $38 \text{ mm} \times 38 \text{ mm}$  active area are mounted on the PST housing, but they are not visible in Fig. 14 because they are located behind the

sample insert. These are used to detect scattering from the smallest three Debye-Scherrer rings, and cover momentum transfers of  $0.25 \leq Q \leq 0.47 \text{ \AA}^{-1}$ . Another lone pencil-style detector with a  $^3\text{He}$  fill pressure of 4 bars and a diameter of 25.4 mm is used to detect neutrons that backscatter from the outer-most Debye-Scherrer ring. These detectors are somewhat off backscattering, resulting in a slightly worsened energy resolution and an asymmetric instrumental resolution function. The larger active area and shorter collimation also lead to a higher background. Both the pencil detectors and the low-angle rectangular detectors perform well in discriminating the neutron signal from the  $\gamma$  background. The background from  $\gamma$  radiation and electronic noise is negligible.

### H. Detector Electronics

The HFBS uses a combined preamplifier-amplifier-discriminator (PAD) unit to process neutron-event signals from each  $^3\text{He}$  detector prior to being counted by a scaler. Several views of the PAD unit are shown in Fig. 15, and the manner in which these units connect to the detector assembly can be seen in Fig. 14. The PAD design is non-trivial as it must comply with a number of constraints. First, the PAD units have to withstand operation under vacuum because the detectors are operated inside the HFBS vacuum chamber, and the PAD units are plugged directly onto the detectors for optimum noise reduction and reliability. Second, the 1/2-inch (12.27 mm) diameter pencil detectors are physically arranged closely together to optimize coverage. This requires the PAD units to have a very flat form factor. Third, the scaler being used has ECL inputs, so the PAD units need to produce a digital output compatible with this standard.

Given that normal convective cooling is not present in a vacuum environment, the first constraint was met by ensuring that the power dissipation in all components was low enough that even the vestigial conduc-



FIG. 14: Picture of the HFBS sample area as viewed from inside the large vacuum chamber, which houses the PST chopper, analyzer, and detector assembly.

tive cooling through the printed circuit board, plus whatever radiative cooling takes place, is sufficient to keep all component operating temperatures within their limits. Two commercial (Amptek) hybrid ICs were chosen to perform most of the PAD functions, the A225 preamplifier/shaping amplifier and the A206 amplifier/discriminator. Both ICs have milliwatt power dissipation and are rated for vacuum operation. The digital output buffer is based on the Telcom TC4428A dual inverting/noninverting driver, a power CMOS part that also shows low power dissipation even when driving heavy loads.

The required flat form factor was reached through careful component selection and package design. The final PAD package thickness is 11.3mm. This was achieved using standard through-hole components, along with easy fabrication and assembly, sturdiness, and adequate shielding. Because the detectors were mounted so closely together, the locking rings on the input SHV plugs had to be cut off. The PAD units (and therefore the SHV plugs which are press-fitted into them) are held in place by a pin that is clamped into the detector mounting plate.

The TC4428A digital output driver produces an inherently balanced TTL-level output. The TC4428A output impedance is so low that the necessary ECL-level outputs can be produced by the unsophisticated but effective method of resistive voltage dividers to the -12V supply. It

is expected that future applications of this driver would use the balanced TTL output and take advantage of the excellent common-mode range of commercial RS485 ICs at the receiving end.

### I. Operational Modes and Data Acquisition

The HFBS employs a “real time” data acquisition system whose primary function is to bin the neutrons counted in each detector according to their incident energy. This energy is determined by the monochromator velocity *at the time the neutron was backscattered from the monochromator*. The data acquisition system also measures the angular velocity and position of the doppler drive cam using a digital encoder, and then calculates the monochromator crystal displacement and velocity. The velocity values are stored in a memory stack, and then used with the displacement values to calculate the neutron flight time to the detectors. This flight time information is used to set stack pointer values that the system will later need to retrieve the correct velocity information when the neutrons are finally counted by the scalers. Further details of these calculations are discussed in Appendix B. During each sampling period, which lasts  $\sim 20 \mu\text{s}$ , the scaler values are latched and read. Using previously calculated pointer values, the incident neutron energy (i.e. monochromator velocity) is retrieved from the velocity stack. The system then increments a histogram using the appropriate incident energy and  $Q$  values. These tasks describe the “standard” operational mode of the HFBS. The data acquisition system also supports an alternative operational mode that allows the user to perform a “fixed window scan” (FWS) for which the doppler drive is stopped and the instrument is simply measuring the elastic intensity as a function of  $Q$ . This mode is generally combined with scans of a physical variable such as sample temperature or time. An example of an FWS spectrum is given in Sec. IV.

A secondary function of the HFBS data acquisition system is to count only those neutrons that backscatter from the analyzer, and to ignore the unwanted neutrons that scatter from the sample directly into the detectors. This function is handled entirely in software, and the timing is controlled by the PST chopper. For each sampling period, the data acquisition system measures the angular position of the PST chopper using a two-pole resolver and then compares it to a look-up table of values to determine if the scaler counts should be kept. To assist in generating this look-up table an alternative operational mode, called “teach” mode, is available that bins the neutrons counted in each detector according to the angular position of the PST chopper. As shown in Fig. 16, the data obtained in teach mode clearly separate the huge signal generated by the unwanted neutrons from the much weaker signal, indicated by the shaded regions, that results from neutrons that have been properly energy-analyzed. Thus “teach” mode is used to in-

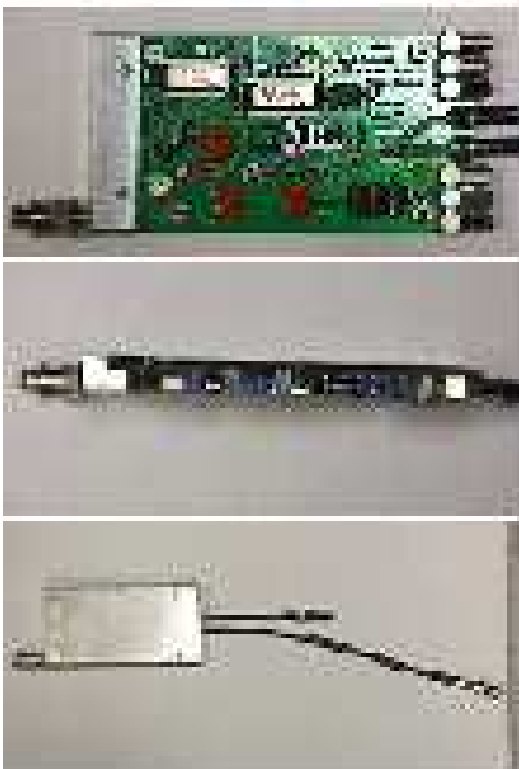


FIG. 15: Three views of the HFBS PAD unit: Top - the bare circuit board, Middle - a side view, Bottom - the complete PAD unit in its casing.

struct the data acquisition system when to keep a neutron count, and when to discard it, based on the angular position of the PST chopper. Figure 16 shows one full period of the PST chopper which, because it rotates at a constant rate of 79 Hz, corresponds to 12.7 msec. The objective of teach mode is then to adjust the positions of the shaded regions to achieve the highest signal-to-background ratio possible.

The HFBS data acquisition system is composed of a number of integral hardware and software components. The main hardware components include a 32-bit VME-compatible single-board computer, a 32-bit latch, a 32-bit high-speed multiscaler, an optical encoder, a resolver-to-digital encoder, and a high-performance digital signal processor. The CPU provides control of the slow processes in the VME data acquisition. The resolver-to-digital encoder system provides a 12-bit digital output corresponding to the angular position of the PST chopper. The latch is used to capture and read the encoded angular position of the PST chopper. The scaler accumulates counts from the neutron detectors and also counts the number of pulses sent from the doppler drive cam optical encoder, which is used to calculate the angular velocity and position of the cam. A high speed digital signal processor (DSP) is used to perform the fast VME readouts of the latch and scaler modules, to calculate the monochromator velocity and displacement, to calculate the pointer values, and also to increment the histogramming memory.

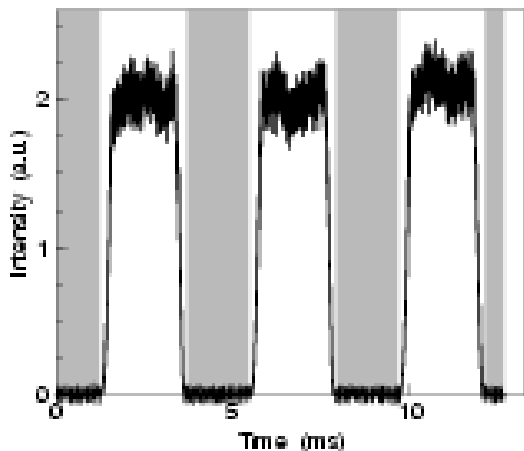


FIG. 16: Neutron intensity during one full cycle of the phase space transformation chopper with the HFBS operating in “teach” mode. The regions of high intensity are caused by monochromated neutrons that scatter from the sample directly into the detectors without energy analysis. Only signals that coincide with the time profile of the analyzed neutrons (shaded areas) are processed by the data acquisition system when operating in the “standard” mode.

## J. Background Reduction

The HFBS design places both sample position and detector assembly in close proximity to the main guide beam (see Fig. 2). This was done to avoid the reflectivity loss and increased beam divergence that would result by diffracting the beam away from the guide using a pre-monochromator. The extra divergence is undesirable because it would reduce the effectiveness of the chopper. The HFBS therefore faces the prospect of having a higher background than those measured at other backscattering spectrometers, where the neutron beams entering the primary spectrometers are usually already pre-monochromated. [8] Furthermore, about  $6.5 \times 10^9$  neutrons per second [14] exit the converging guide and fly towards the PST chopper. When this rate is compared to the single-detector count rate of a few counts per second typical for a standard experiment, the need for extensive background reduction is obvious.

A number of measures have been taken to reduce the HFBS background as much as possible. Several of these have already been discussed, such as the use of liquid-nitrogen-cooled beryllium and bismuth filters, which reduce the fast neutron background component, and the velocity selector, which limits the wavelength bandwidth seen by the PST chopper. The background is further reduced by continuously flushing the flight path between the monochromator and the PST chopper with He gas. This process eliminates air scattering, which for dry air is 7.3% per meter, and leads to an increase in the detector signal. A system of masks made of absorbing boronated aluminum (Al loaded with  $\sim 5\%$   $^{10}\text{B}$ ) are used to define the entrance and exit of the PST chopper window so that neutrons exiting the converging guide are either absorbed by the masks, or hit the rotating HOPG crystals. Neutrons incident on the HOPG crystals are then either diffracted, or transmitted. To absorb those neutrons that are transmitted, a 2 mm thick layer of boron in epoxy, molded to the shape of the cassettes, is positioned immediately behind the crystals. This boron in epoxy layer also functions as a beam stop when one of the three cassettes has rotated into the beam path. This is quite important because, as seen in Fig. 16, the data acquisition system is processing signals from the detectors precisely at this time. When none of the crystal sections is in the beam, the incoming neutrons are absorbed directly after the PST chopper by a beam stop made from a  $^6\text{Li}$ -bearing ceramic. An additional slit system positioned between the chopper and sample position leads to a further reduction in background. Finally, the stainless steel housing of the PST chopper is itself completely covered with boronated aluminum and an outer layer of cadmium.

The dominant contribution to the background, in spite of the features listed above, comes from the leakage of neutrons through the chopper exit window during the time a crystal cassette is blocking the beam path. We attribute this to multiple scattering of neutrons within

the chopper housing. However, this contribution drops by a factor of 3 when the HFBS scattering chamber is evacuated and the chopper entrance and exit windows (1 mm thick aluminum) are removed, which is the standard operating mode for the HFBS. At the same time we observe a 22 % increase in the scattering signal. The HFBS scattering chamber can be evacuated with a large mechanical roughing pump to a vacuum of better than  $10^{-2}$  mbar in less than 4 hours, at which pressure the high voltage to the detectors can be switched on.

#### IV. PERFORMANCE

A gold foil activation measurement at the sample position gives a flux of monochromated neutrons on the sample at  $E_0$  of  $1.4 \times 10^5 \text{ n}(\text{cm}^2 \text{ sec})^{-1}$ . [14] The beam size at the sample position has been measured by irradiating a 125  $\mu\text{m}$  thick Dy foil. The autoradiograph image is consistent with a beam size of 2.9 cm  $\times$  2.9 cm, and a uniform beam intensity profile.

Figure 17 shows the spectrum of an annular vanadium standard with an outer diameter of 22 mm, and a wall thickness of 0.88 mm. This geometry yields a 10 % scatterer. The spectrum was taken at room temperature with the Doppler drive operating at a frequency of 13.5 Hz, corresponding to a dynamic range of  $\pm 30 \mu\text{eV}$ . The average count rate in each detector was 106 counts per minute. The spectrum is shown using a logarithmic representation to show the Gaussian nature of the vanadium spectrum more clearly. For this standard we observed a signal-to-background ratio of better than 400:1. Measurements on materials having a lower cross section for absorption than that of vanadium (e.g. samples with

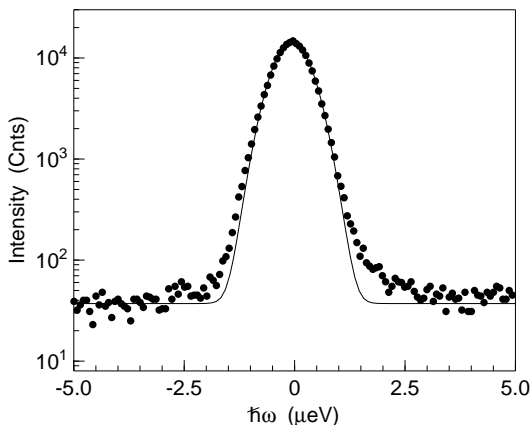


FIG. 17: Standard vanadium spectrum measured on the HFBS using a Doppler drive frequency of 13.5 Hz ( $\pm 30 \mu\text{eV}$ ), and integrating over  $0.62 \leq Q \leq 1.6 \text{ \AA}^{-1}$ . The solid line represents a fit to a Gaussian function plus a constant background  $bg + a \exp[-(x/b^2)]$ . The spectrum shows an almost Gaussian-like energy resolution with a FWHM of  $0.93 \mu\text{eV}$ . Extensive efforts at background reduction have led to a signal-to-background ratio ( $a/bg$ ) of better than 400:1.

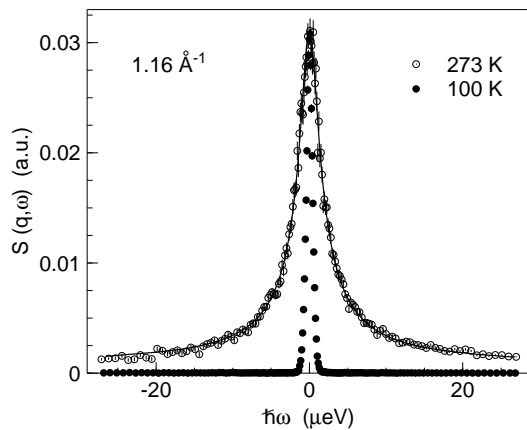


FIG. 18: Dynamics of glass-forming dibutylphthalate at  $1.16 \text{ \AA}^{-1}$ . Structural relaxation leads to a quasielastic broadening in the scattering law  $S(q, \omega)$  with increasing temperature which can be described by the Fourier transform of a Kohlrausch stretched exponential function (solid line). The spectrum at 100 K – representing the instrumental resolution – has been scaled down by a factor of 18 to match  $S(q, \omega=0; 273 \text{ K})$ .

a high hydrogen content) give signal-to-background ratios as high as 600:1. Up to Doppler-drive frequencies of 16.2 Hz ( $|\Delta E| \leq 36 \mu\text{eV}$  for the triangular cam), all HFBS spectra exhibit Gaussian-like energy resolution lineshapes.

One of the main applications of neutron backscattering spectroscopy is the study of slow atomic motions in viscous liquids. In a first experiment the structural relaxation in glass-forming dibutylphthalate was measured at temperatures from 100 K to 273 K using a closed cycle refrigerator. [25] Liquid dibutylphthalate was encapsulated inside a hollow aluminum cylinder 25 mm in diameter, 75 mm in length, having an annular thickness of 0.08 mm. This geometry also yields a 10 % scatterer. The spectra shown in Fig. 18 have been normalized to the monitor and the vanadium standard, and also corrected for a flat background and empty-cell scattering. The measuring time at 273 K was 7 hours at a count rate of 76 counts per minute per detector (119 counts per minute per detector at 100 K). Structural relaxation, which is responsible for viscous flow, broadens the quasielastic linewidth with increasing temperature. Typical for glass-forming systems is the stretching of correlation functions over a wider time scale than is expected for exponential relaxations. This is an example of a system for which the extended dynamic range of the HFBS is especially valuable as it permits the study of structural relaxation in viscous liquids in greater detail.

The relaxation of the Si-O network in sodium disilicate [26] was studied at temperatures up to 1600 K using the HFBS high temperature furnace. Due to the chemical reactivity of liquid silicate glasses, a platinum sample holder had to be used. The neutron absorption cross section of platinum at  $\lambda = \lambda_0$  is 35.9 barns. This is about

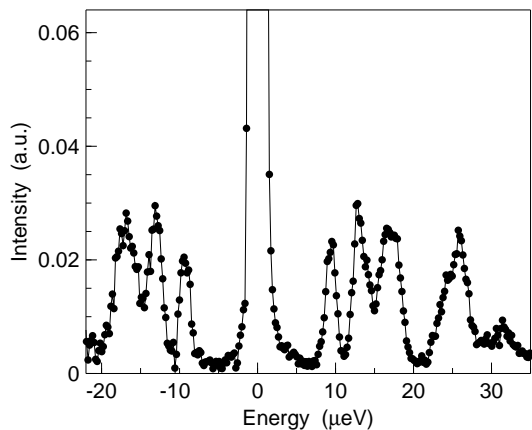


FIG. 19: Tunneling spectrum of 2,6-Lutidine illustrating the large dynamic range of the HFBS ( $\pm 36 \mu\text{eV}$ ), and an energy resolution of  $1.01 \mu\text{eV}$  (FWHM).

45 times larger than that of aluminum. This large cross section is even more problematic given that the beam passes through the sample twice on its way to the detectors. Even so, the high flux provided by the HFBS resulted in a count rate of some 13 counts per minute per detector, still enough for quantitative data analysis.

A recent measurement of the tunnel splitting in 2,6-Lutidine ( $\text{C}_7\text{H}_9\text{N}$ ) served as a test of the large dynamic range of the HFBS as well as the excellent energy resolution. This system had been examined on a number of spectrometers including a backscattering instrument. [27] Due to the large number of peaks in the spectrum at energies less than  $50 \mu\text{eV}$ , some of which overlap, this system has also been used as a test case for maximum entropy [28] and Bayesian analysis techniques. [29, 30] The data, summed over 10 detectors spanning  $0.62 \text{ \AA}^{-1}$  to  $1.6 \text{ \AA}^{-1}$ , and normalized to the incident beam monitor spectrum, are shown in Fig. 19.

As discussed in Sec. IIII, the backscattering spectrom-

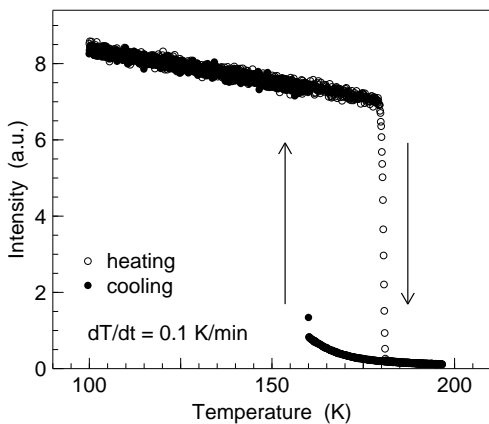


FIG. 20: A fixed-window scan of toluene that clearly shows supercooling. The heating and cooling rates used in this measurement were both  $\pm 0.1 \text{ K/min}$ .

eter can also be operated with the Doppler monochromator at rest, in which case it probes only the energy-resolution-limited elastic scattering intensity. The FWS method is a useful technique for determining under what conditions (e.g. temperature, time) the dynamics of the system being studied lie within the dynamic range of the spectrometer. [31] In addition, this technique can be useful for probing phase transitions. As an example of this, the heating and cooling curves for toluene are presented in Fig. 20. In this figure, the data were summed over 10 detectors and warming/cooling rates of  $\pm 0.1 \text{ K/min}$  were used. The large hysteresis on heating and cooling, indicative of undercooling, is clear. The solid melts at 179 K and the liquid solidifies at about 160 K.

## V. UPGRADES AND PROSPECTS

In March of 2002, work was completed on the installation of a new cold source into the NCNR research reactor. The complex shape of the new source, which is an ellipsoidal shell, allows more  $\text{D}_2\text{O}$  to be introduced in the cryostat chamber than did the spherical shape of the old cold source. [10, 32] This modification provides the single biggest contribution to the overall gain in cold neutron flux. The center of the inner ellipsoid is also offset, so that the thickness of liquid hydrogen nearest the source of neutrons is 30 mm, as compared to 20 mm in the original source. Finally, the inner ellipsoid is held under vacuum, whereas the inner shell of the old source was filled with hydrogen-vapor. The overall flux gains range from 40% at  $2.4 \text{ \AA}$  to slightly more than 100% for wavelengths greater than  $15 \text{ \AA}$ . For the HFBS, the new cold source has increased the usable flux at  $\lambda_0$  by a factor of 1.8, precisely in line with expectations. [32] With this cold source upgrade, the HFBS currently provides a neutron flux on sample of  $2.5 \times 10^5 \text{ n (cm}^2 \text{ sec)}^{-1}$ , which is higher than that of any other backscattering spectrometer operating on a steady state source.

Several ideas for improving the HFBS have been considered and evaluated in detail. These include a new parabolic converging guide [33] with a focal point that is centered on the PST chopper HOPG crystals, and a supermirror guide section that functions as an optical filter. While a new parabolic converging guide is mainly expected to improve the signal-to-background ratio, an optical filter would shift the HFBS out of the direct line-of-sight of the neutron source, and thus allow for the removal of the beryllium and bismuth filters. The replacement of these filters with an optical filter could produce a substantial enhancement of the incident neutron flux on the sample.

## VI. SUMMARY

The primary goal of the HFBS is to provide a sub- $\mu\text{eV}$  energy resolution capability to the NCNR scatter-

ing community while maximizing the flux on sample as well as the dynamic range. To this end the HFBS design incorporates several state-of-the-art neutron optic, mechanical, and electronic devices. Foremost among these is the phase space transformation chopper which converts the energy spread of the neutron beam exiting the converging guide into one that is highly divergent but more densely distributed about the backscattered energy of 2.08 meV. This device has operated flawlessly for over four years and enhances the neutron flux by a factor of 4.2. In addition, a considerable increase in signal is achieved using a 4 m long converging guide section and a large analyzer that subtends nearly 23% of  $4\pi$  steradians.

In contrast to other backscattering spectrometers, the HFBS employs a high-speed, cam-based Doppler-drive system to vary the incident energy  $E_i$  up to  $\pm 50 \mu\text{eV}$ . The shape of the cam is machined to produce a nearly triangular velocity profile for the monochromator. In routine operation the monochromator system provides a Gaussian-like sub- $\mu\text{eV}$  instrumental energy resolution for energy transfers of up to  $\pm 36 \mu\text{eV}$ . Routine user operation began in late 1999. Since then the HFBS has proven to be a reliable instrument. Up to now more than 90 successful experiments, using temperatures ranging from 2 K to 1600 K, have been performed by users from university, industrial, and research centers. At present requests for beam time on the HFBS exceed the available time by a factor of 1.8. The HFBS design and performance have led to sizable enhancements in both neutron flux and dynamic range compared to that available on other reactor-based backscattering instruments.

### Acknowledgments

The design and construction of the NIST Center for Neutron Research HFBS spectrometer has been the result of an intense collaboration between many scientists, engineers, technicians, and computer programmers. It would not be the success that it is without the considerable expertise and efforts of the following support staff: Technical - G. M. Baltic (head technician), A. Clarkson, D. Clem, W. Clow, M. J. Rinehart, and S. Slifer; Engineering - P. Brand (Doppler drive system), C. Brocker (PST chopper, vacuum chamber, and detector assembly), R. Christman (Doppler drive and detector assembly), A. E. Heald (guide shielding), J. LaRock (cryogenic inserts), J. Moyer (vacuum chamber shielding), D. Pierce (velocity selector mount and neutron shutter), I. G. Schröder (neutron guides and shielding); Electrical - B. Dickerson (PLC system), D. Kulp, T. Thai, J. Ziegler (detector electronics); Computer - N. C. Maliszewskyj (data acquisition software). In addition, the following scientists were involved with various aspects of the design, construction, and testing phases of the instrument development: Z. Chowdhuri, J. C. Cook (Monte Carlo simulations), K. T. Forstner (HOPG crystal tests), P. D. Gallagher (data acquisition hardware and software), and C. Karmonik (PST

chopper tests, background reduction, and software development). Special mention is due to C. Appel (analyzer and monochromator) and B. Frick (IN16 analyzer tests), both of whom contributed enormously towards the realization of the HFBS. The authors finally wish to express their sincere thanks for the many helpful and stimulating discussions with B. Alefeld, B. Frick, A. Heidemann, O. Kirstein, A. Magerl, M. Popovici, M. Prager, J. M. Rowe, and J. J. Rush.

### APPENDIX A: PHASE SPACE TRANSFORMATION

The function of the PST chopper is to transform the shape of an incoming neutron beam in phase space such that the neutron flux of the outgoing diffracted beam is enhanced at the backscattering energy  $E_0 = 2.08 \text{ meV}$ . This idea was developed by Schelten and Alefeld to address the severe mismatch in divergence between primary and secondary spectrometers. [18]

Figure 5 provides a phase space diagram that outlines the operating principle behind the phase space transformation chopper. The incoming neutron beam has a relatively small angular divergence that is set by the critical wave vector  $Q_c$  of the guide coatings, (Sec. IIIB) but a substantial spread in wave vector  $\Delta k$  ( $k = 2\pi/\lambda$ ). After diffracting from the (002) Bragg reflection of a mosaic HOPG crystal at rest, the outgoing phase space element has a much broader divergence (see Fig. 5(a)). Figure 5(b) demonstrates what happens when the HOPG crystal is set in motion parallel to  $-\vec{k}_x$  at a linear speed of 250 m/s. The outgoing phase space element is now both larger and more divergent. More importantly, it is tilted such that its arc is essentially perpendicular to  $k_f$ . This tilt produces a much narrower energy spread about  $E_0$ .

Analytic calculations of the gain from phase space transformation (PST) can be made under certain simplifying assumptions, and provide extremely useful guidance in the optimization of different physical parameters. The geometry for the diffraction process from the moving lattice is shown in Fig. 21 (reproduced from [18]). Previous calculations by Schelten and Alefeld were performed for the gain under different crystal and spectrometer configurations, but were done assuming the *optimal* crystal velocity [18]. Below we describe how the analytic equations can be extended to arbitrary crystal velocities.

As presented in [18], the angle the diffracted phase space element makes with respect to the horizontal axis is written as

$$\tan \chi = \frac{\tan \theta_g}{2 \tan \theta_g \tan \theta + 1}, \quad (\text{A1})$$

where  $\theta_g$  is the incident angle in the laboratory frame and  $\theta$  is the incident angle in the moving crystal frame.  $\theta_g$  is given by the  $d$ -spacing of the moving crystal (in this case graphite, hence the subscript “g”) and the desired



wavelength  $\lambda_0$  via Bragg's law,  $\theta_g = \sin^{-1}(\frac{\lambda_0}{2d})$ . The velocity in the crystal system is determined by

$$V_K = v_0 \sin \theta_g [\cot \theta_g - \cot \theta], \quad (\text{A2})$$

where  $V_K$  is the velocity of the crystal and  $v_0$  is the velocity of the neutron corresponding to the desired neutron wavevector  $k_0$ :

$$m_n v_0 = \hbar k_0. \quad (\text{A3})$$

Equation (A2) is obtained from the geometry in Fig. 21 by noting that  $k_0 \sin \theta_g = k^* \sin \theta$  and  $k^* \cos \theta = K + k_0 \cos \theta_g$ , where  $\hbar K = m_n V_K$ .

We can solve Eq. (A2) for  $\theta$  with the following result:

$$\tan \theta = [\cot \theta_g + \frac{V_K}{v_0 \sin \theta_g}]^{-1}. \quad (\text{A4})$$

From Eqs. (A4) and (A1) we can determine the tilt angle,  $\chi$ , of the scattered phase space element.

From the incident phase space element we can use the geometry illustrated in Fig. 21 to relate the length of the element,  $\Delta k$ , to the quantities known so far. In terms of the mosaic spread,  $\varepsilon$  (HWHM), (assumed known) we have

$$\tan \varepsilon = \frac{\Delta k \sin \theta_g}{K + \Delta k \cos \theta_g + k_0 \cos \theta_g}, \quad (\text{A5})$$

which can be solved for  $\Delta k$ ,

$$\Delta k = \frac{K + k_0 \cos \theta_g}{\cot \varepsilon \sin \theta_g - \cos \theta_g}. \quad (\text{A6})$$

We can also find the projection of the incident phase space element onto the vertical axis to obtain

$$\begin{aligned} y &= \Delta k \sin \theta_g \\ &= \frac{(K + k_0 \cos \theta_g) \sin \theta_g}{\sin \theta_g \cot \varepsilon - \cos \theta_g}. \end{aligned} \quad (\text{A7})$$

We also note that the divergence of the incident beam,  $\eta$ , and the incident beam wavevector,  $k_0$ , determine the width of the incident phase space element  $\delta k$  via

$$\delta k = \eta k_0. \quad (\text{A8})$$

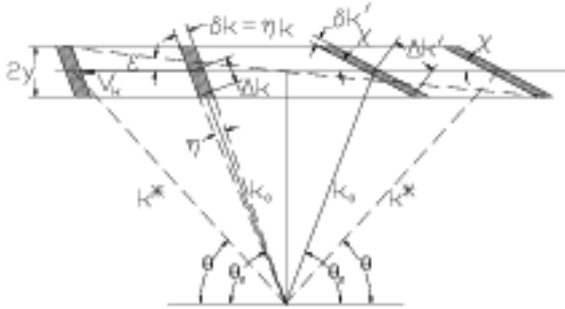


FIG. 21: Phase space geometry for Bragg diffraction from a moving crystal with mosaic  $\varepsilon$  (HWHM).

The volume of the incident phase space element is given by

$$V_{ps} = 2\Delta k \delta k. \quad (\text{A9})$$

Since the phase space volume for the incident and scattered neutrons must be equal by Liouville's theorem, we have

$$\begin{aligned} V_{ps} &= 2\Delta k \delta k \\ &= 2\Delta k' \delta k'. \end{aligned} \quad (\text{A10})$$

From the geometry of the scattered phase space element we have

$$y = \Delta k' \sin \chi, \quad (\text{A11})$$

which can be solved for  $\Delta k'$  since we know  $\chi$  and  $y$  from Eqs. (A1) and (A7) respectively,

$$\Delta k' = \frac{y}{\sin \chi}. \quad (\text{A12})$$

Using Eqs. (A10) and (A12) we can express  $\delta k'$  in terms of the known quantities,

$$\delta k' = \frac{V_{ps} \sin \chi}{2y}. \quad (\text{A13})$$

A magnified view of the scattered phase space element is illustrated in Fig. 22. In particular we show how the monochromator (placed after the PST chopper) will intersect the phase space element. Note that at the optimal velocity this line will be parallel to the long axis of the phase space element and the neutron intensity gain will be a maximum. From the geometry shown in Fig. 22, the angle  $\alpha$  is given by  $\alpha = \chi + \theta_g + \frac{\pi}{2}$ . The projection of the monochromator intersection with the phase space element is given by  $\min(d, 2\Delta k')$  where  $d$  is given by the geometry shown,

$$d = \frac{\delta k'}{\sin \alpha}. \quad (\text{A14})$$

The gain of the PST chopper is then given by the ratio of the final phase space width (as seen by the monochromator) to the initial phase space width defined in Eq. (A8),

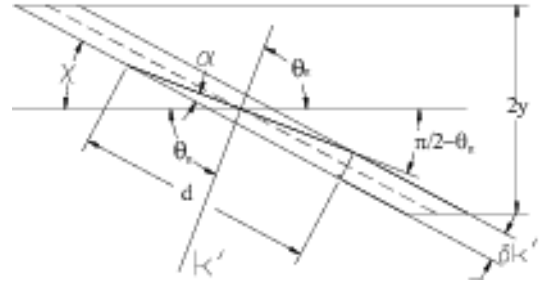


FIG. 22: Magnified view of the Bragg-reflected phase space element.

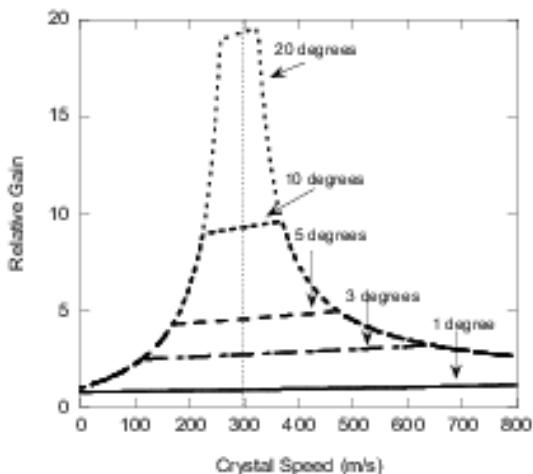


FIG. 23: Relative gain in neutron flux as a function of crystal speed for several different values of mosaic spread based on Eq. (A15). The simulations assume a wavelength of  $\lambda_0$ .

and is expressed in terms of the known quantities

$$gain = \frac{\min(d, 2\Delta k')}{\eta k}. \quad (\text{A15})$$

Fig. 23 shows the calculated gain as a function of crystal speed over a large range of mosaic spreads,  $2\epsilon = 1^\circ, 3^\circ, 5^\circ, 10^\circ$  and  $20^\circ$ . For mosaics of  $3^\circ$  and larger, the gain increases rapidly from one at low speeds, but then abruptly enters a linear region at a mosaic-dependent speed. At higher speed, the linear region abruptly ends and the gain decreases smoothly from this point on. For each mosaic value except  $2\epsilon = 1^\circ$ , the gain curves lie on top of each other at sufficiently low and high crystal speeds. The only difference is the location of the linear region that clips the top of the curve. The gains for this linear region increase with increasing  $2\epsilon$ , whereas the width of the region shrinks. The linear region occurs when  $\min(d, 2\Delta k') = 2\Delta k'$  (see Fig. 22), which happens to be satisfied for the case  $2\epsilon = 1^\circ$  over the entire crystal speed range shown. This happens because the mosaic of  $1^\circ$  is too small compared to the divergence of the incident beam. The maximum gain found here (19.5) occurs for the largest mosaic of  $20^\circ$  at a crystal speed of 320 m/s. Note however that the reflectivity of the moving crystals has been assumed constant for all cases of mosaic spread, an assumption that is incorrect for real crystals. In fact, at a constant thickness the reflectivity of real crystals decreases with increasing mosaic spread. In addition, these calculations assume a  $k$ -independent, or constant energy spectrum incident on the PST chopper, when in fact the cold source produces a Maxwell-Boltzmann neutron energy distribution, which is further modified by the guide coatings and filters downstream. These and other simplifications will cause the actual gain value to be less than that found in this analytical calculation.

This analytical analysis quickly gives one a very good intuitive feel for the relative gains one can expect from

various experimental configurations. However, as mentioned above, the calculations make several approximations, all of which tend to overstate the gain, and which result in the chopped-off appearance of the different gain curves. The most important of these approximations treats the scattered phase space element as a parallelogram when in fact it is a rather complicated crescent-shaped surface (see Fig. 5). Moreover, the locus of final wavevectors accepted by the monochromator collectively describe the surface of a sphere. Thus, instead of the gain being given by the intersection of a line with a parallelogram, it should be given by the intersection of these two more complicated curved surfaces. (The word “surface” is slightly misleading because both objects actually have non-zero width along  $k$ .) This will tend to round the shape of gain curves and reduce the gain, particularly at high speeds, due to the mismatch between the shape of the phase space element accepted by the monochromator and that diffracted by the PST chopper. To account for these complex geometrical effects, as well as the reflectivity dependence on mosaic spread and the true energy spectrum seen by the PST chopper, Monte Carlo simulations of the phase space transformation chopper have been performed.

The PST chopper is located immediately after the converging guide described in Sec. III B, the supermirror coatings of which have a critical angle of about twice that of  $^{58}\text{Ni}$ . Based on simulations, the divergence after this element was taken to be  $2.8^\circ$  in the horizontal plane and  $4.4^\circ$  in the vertical direction. The HOPG crystals were chosen to have a thickness of 5 mm. The incident neutron energy spectrum was chosen to be a 65 K Maxwell-Boltzmann distribution, in accord with measurements of the flux from the NIST cold source, but truncated at 4 Å to simulate the effect of a beryllium filter in the incident beam. The spectrum was also truncated at 10 Å because wavelengths longer than this have no probability of being diffracted by the moving crystal. This distribution was then multiplied by the square of the incident wavelength in order to account for the fact that the critical angle for total external reflection is proportional to the wavelength. The simulation included both horizontal and vertical mosaics, and the velocity of the graphite crystal. The program randomly chose the incident wavelength, the angles of incidence (within limits given by the divergences stated above), and the vertical orientation of the crystallite involved in the Bragg reflection. These parameters were sufficient to determine the horizontal orientation required for diffraction to occur. In addition the reflectivity of the graphite was included via the Bacon-Lowde equation for diffraction from ideally imperfect crystals. [23] The HOPG crystals used in the PST chopper are most likely not all “ideally imperfect.” Thus even this more realistic assumption still overestimates the reflectivity of the HOPG crystals, and produces simulated gains larger than what are actually observed. All of these simulations have been performed using silicon (111) crystals as the monochromator.

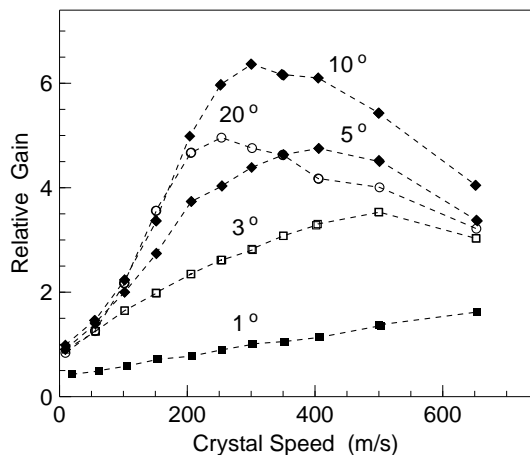


FIG. 24: Simulations of the relative gain in neutron flux as a function of crystal speed for several different values of mosaic spread (numbers are FWHM). The simulations assume a 5 mm thick crystal and a wavelength of  $\lambda_0$ .

Two-dimensional projections of simulated Bragg reflections from an HOPG crystal having an isotropic  $10^\circ$  mosaic are shown in Fig. 5 for three different crystal speeds. A coordinate system is used in which the  $(x, y)$  plane coincides with the horizontal scattering plane, and the  $y$ -axis is oriented antiparallel to the  $(002)$  scattering vector. The incident and final  $k_x$  and  $k_y$  values of the diffracted neutrons are represented by individual dots, while the value of  $k_z$  is neglected. This results in dots whose total  $k$  vectors seem abnormally short. The reference values of  $k_x$  and  $k_y$  are indicated by the solid lines. Two effects are evident in these simulations. The first is that the phase space element volume increases as the crystal velocity (oriented opposite  $k_x$ ) increases, in agreement with the analytic calculations. This is because the Bragg reflection takes place at a lower angle in the Doppler frame. The second is that the diffracted element tilts in phase space as the crystal velocity is changed. This tilt can be optimized to maximize the number of neutrons that have the correct energy to be backscattered from a Si  $\{111\}$  crystal.

The simulated flux gain, calculated using the same parameters as the analytical gain shown in Fig. 23, is shown in Fig. 24. As in the analytical calculation, the peak intensity (relative to that obtained for a crystal velocity of zero) is shown as a function of speed for mosaics  $2\varepsilon = 1^\circ, 3^\circ, 5^\circ, 10^\circ,$  and  $20^\circ$ . There are a number of similarities between the simulation and the analytical calculation. For mosaics of  $3^\circ$  or larger, the relative intensity increases from about 1 to a broad maximum, before decreasing again. For the parameters chosen here, the maximum gain ( $\sim 6$ ) occurs for a crystal with a  $10^\circ$  mosaic moving at about 300 m/s. The results for a  $20^\circ$  crystal show a smaller gain due to a lower reflectivity. As in the analytical calculation, the gain for the  $1^\circ$  mosaic case increases linearly with crystal speed, and has a relative value of less than one for zero speed.

Phase-space transformation is an ideally suited method for boosting the count rates on backscattering instruments because it increases the divergence of the diffracted beam at the same time, thus alleviating the mismatch in angular acceptance between the monochromator and analyzer systems. However, there are several considerations that limit how far one can take the PST process. For example, a PST chopper using  $10^\circ$  mosaic crystals, which in our simulations resulted in the highest gain, would produce a beam with a horizontal divergence that is slightly larger than the  $20^\circ$  expected. To accept and use all of this divergence would require a monochromator approximately 75 cm long. This would imply a heavy monochromator assembly, and present serious technical challenges related to the Doppler drive system. Thus we compromised on a more reasonable monochromator length of 52 cm and a mosaic of about  $7.5^\circ$ . We also reduced the operational velocity of the PST chopper to 250 m/s to make the forces on the composite disk more manageable and increase the reliability. Given these compromises, our simulations predict that the gain from the PST should be about a factor of 5. This can be compared to the gain of 6.7 calculated in the analytical formulation using the same parameters, and agrees quite well with the experimentally measured value of 4.2.

## APPENDIX B: FLIGHT TIME OFFSET CORRECTIONS

In this appendix we discuss the flight-time offset corrections (FTOSC). In particular we show that when the amplitude and velocity of the monochromator are appreciable, parts of the spectrum undergo an apparent shift. It turns out that the elastic lineshape is affected the most whereas scattering features at the largest energy transfers are affected only marginally.

A schematic of the relevant instrument geometry is presented in Fig. 25. The velocity of the neutrons reflected from the Doppler monochromator is a time-dependent quantity,  $v_n(t)$ . The velocity of the monochromator,  $v(t)$ , modulates the reflected velocities about the Bragg velocity,  $v_0$ , so that the neutrons that strike the sample have a velocity  $v_n(t) = v_0 + v(t)$ . For a sinusoidal monochromator motion with an amplitude of 4.5 cm and a frequency of 25 Hz, the maximum monochromator speed is 7.07 m/s. Thus the neutron velocity varies between 632.7 m/s and 637.9 m/s.

The arrival time in the detectors,  $t_d$ , of the neutrons that scattered from the monochromator at time  $t$  is given by

$$t_d = t + \frac{d_{sad}}{v_0} + \frac{d_{ms} + x(t)}{v_0 + v(t)}, \quad (\text{B1})$$

where the sample-analyzer-detector distance is  $d_{sad} = d_{sa} + d_{ad}$ ,  $d_{ms}$  is the sample-monochromator distance, and  $x(t)$  is the monochromator displacement (see Fig. 25). If we were to neglect the motion of the

monochromator in calculating the arrival time ( $x(t) = 0, v(t) = 0$ ) we obtain the zero-monochromator motion arrival time,

$$t_0 = t + \frac{d_{sad} + d_{ms}}{v_0}. \quad (\text{B2})$$

The actual arrival time,  $t_d$ , can be rewritten in terms of  $t_0$  as follows,

$$t_d = t_0 + \delta t, \quad (\text{B3})$$

where

$$\delta t = \frac{d_{ms}}{v_0} \frac{\frac{x}{d_{ms}} - \frac{v}{v_0}}{1 + \frac{v}{v_0}}. \quad (\text{B4})$$

This term,  $\delta t$ , is the flight-time offset correction term. Note that it only becomes important for large values of the quantities  $x/d_{ms}$  and  $v/v_0$ . The large-amplitude/high-frequency operation of the HFBS Doppler monochromator yields non-negligible values for  $\delta t$ . To appreciate the magnitude of  $\delta t$  under routine operating conditions on HFBS, let us assume that the monochromator frequency is 17.7 Hz (corresponding to a dynamic range of  $\pm 33 \mu\text{eV}$ ). At maximum monochromator velocity,  $v = 5 \text{ m/s}$  and  $x = 0$ . At zero velocity,  $x = 0.045 \text{ m}$ . Using  $d_{ms} = 2.25 \text{ m}$ ,  $v_0 = 630.8 \text{ m/s}$ , and  $d_{sad} = 4.12 \text{ m}$ , we obtain  $\delta t = -28 \mu\text{s}$  at maximum monochromator velocity, while  $\delta t = 71 \mu\text{s}$  at zero monochromator velocity. Since the cam that moves the

monochromator rotates at a uniform rate, constant cam intervals are also constant time intervals. With constant time bins of  $20 \mu\text{s}$  (the smallest time bin in the HFBS data acquisition configuration), parts of the spectrum can be shifted by as much as three channels. However, since  $\delta t$  varies, different portions of the spectrum will be affected differently.

One is usually interested in a spectrum in energy, not time-of-arrival. Therefore we can also calculate the implications for the energy when the FTOSC time is used in the data acquisition and when it is ignored. When the motion of the monochromator is ignored in the time-of-arrival in the detectors, the time-dependence of the energy of the neutron after reflection from the monochromator is given simply by

$$E_n^{nofosc} = E(t_0). \quad (\text{B5})$$

If we take into account the FTOSC term then

$$E_n^{fosc} = E(t_0 + \delta t). \quad (\text{B6})$$

To first order we may expand this expression out in  $\delta t$ ,

$$E_n^{fosc} = E(t_0) + \delta t \frac{\partial E}{\partial t} \Big|_{t_0} \quad (\text{B7})$$

$$= E + \delta E. \quad (\text{B8})$$

Thus for small values of  $\delta t$ , the spectrum will be shifted by an amount proportional to  $\delta t$ . In our case with  $f_{Dop} = 17.7 \text{ Hz}$ , we find  $\delta E = 0.3 \mu\text{eV}$ , or roughly one third of the instrumental resolution. When  $E$  is a maximum,  $\partial E / \partial t$  is zero, resulting in no shift.

The spectral lineshape will also be distorted since the Jacobian in the nonlinear transformation is not unity, although this is a much weaker effect than the shift. As is the case with the shift, the distortion is most pronounced at the elastic peak position, where the monochromator velocity is zero, and smallest when the monochromator speed is maximum.

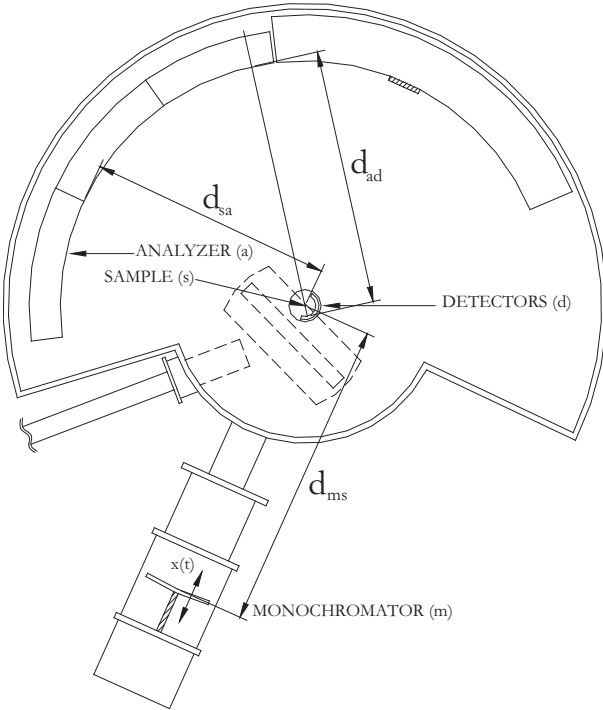


FIG. 25: Schematic diagram of the relevant instrument geometry which provides the definition of terms used in the FTOSC.

- 
- [1] H. Maier-Leibnitz, *Nukleonik* **8**, 61 (1966).
- [2] B. Alefeld, Bayer. Akademie der Wissenschaften, Math. Naturwiss. Klasse **11**, 109 (1966).
- [3] V. E. Bottom, *Anais da Academia Brasileira Ciêneas* **37**, 407 (1965).
- [4] C. G. Darwin, *Phil. Mag.* **27**, 315 and 675 (1914); P. P. Ewald, *Z. Phys.* **30**, 1 (1924).
- [5] M. Birr, A. Heidemann, and B. Alefeld, *Nucl. Instr. Methods* **95**, 435 (1971).
- [6] G. Basile, A. Bergamin, G. Cavagnero, E. Vittone, and G. Zosi, *Phys. Rev. Lett.* **72**, 3133 (1994).
- [7] J. C. Cook, W. Petry, A. Heidemann, and J-F. Barthélemy, *Nucl. Instr. and Meth.* **A312**, 553 (1992).
- [8] Yellow Book ILL.
- [9] P. M. Gehring and D. A. Neumann, *Physica B* **241–243**, 64 (1998).
- [10] R. E. Williams, J. M. Rowe, and P. Kopetka, *Proceedings of the International Workshop on Cold Moderators for Pulsed Neutron Sources*, Argonne National Laboratory, Sept. 29 - Oct. 2, 1997, J. M. Carpenter and E. B. Iverson, editors, pp. 79-86.
- [11] C. F. Majkrzak and J. F. Ankner, in *Neutron Optical Devices and Applications*, C. F. Majkrzak and J. L. Wood, eds. SPIE Proc. Vol. 1738, (SPIE, Bellingham, WA, 1992) p. 150.
- [12] L. A. de Graaf, IRI report 132-82-02/1, (1984).
- [13] C. J. Glinka, private communication.
- [14] This number should be multiplied by 1.8 to account for the increased cold neutron flux provided by the new hydrogen cold source described in Sec. V.
- [15] I. S. Anderson, in *Thin-Film Optical Devices: Mirrors, Supermirrors, Multilayer Monochromators, Polarizers and Beam Guides*, ed. C. F. Majkrzak, *Proc. SPIE* **983**, 84 (1989).
- [16] J. R. D. Copley, *J. Neutron Research* **1**, 21 (1993).
- [17] J. C. Cook, private communication.
- [18] J. Schelten and B. Alefeld, in *Proc. Workshop on Neutron Scattering Instrumentation for SNQ*, edited by R. Scherm and H. H. Stiller, report Jül-1954 (1984); G. S. Bauer and R. Scherm, *Physica B* **136**, 80 (1986).
- [19] S. M. Shapiro and N. J. Chesser, *Nucl. Instr. and Meth.* **101**, 183 (1972).
- [20] C. G. Shull and N. S. Gingrich, *J. Appl. Phys.* **35**, 678 (1964); B. Buras and T. Giebultowicz, *Acta Cryst.* **A 28**, 151 (1972); D. Bally, E. Tarina, and N. Popa, *Nucl. Instr. and Meth.* **127**, 547 (1975).
- [21] A. D. Stoica and M. Popovici, *J. Appl. Cryst.* **22**, 448 (1989).
- [22] The etching was done in a 10% solution of HF acid.
- [23] G. E. Bacon and R. D. Lowde, *Acta Cryst.* **1**, 303 (1948).
- [24] M. Popovici, private communication.
- [25] A. Meyer et al., to be published.
- [26] A. Meyer, H. Schober, D. B. Dingwell, *Europhys. Lett.* (in press).
- [27] F. Fillaux, C. J. Carlile, G. J. Kearley, M. Prager, *Physica B* **202**, 302 (1994).
- [28] R. Mukhopadhyay, C. J. Carlile, R. N. Silver, *Physica B* **174**, 546 (1991).
- [29] D. S. Sivia and C. J. Carlile, *J. Chem. Phys.* **96**, 170 (1992).
- [30] D.S. Sivia, *Physica B* **202**, 332 (1994).
- [31] T. Springer, in *Dynamics of Solids and Liquids by Neutron Scattering*, eds. S.W. Lovesey and T. Springer, (Springer-Verlag, Berlin Heidelberg, 1977) p. 284.
- [32] R. E. Williams and J. M. Rowe, *Physica B* **311**, 117 (2002); For current performance information refer to <http://www.ncnr.nist.gov/coldgains/>.
- [33] P. Böni, private communication.